Improvement of the modal expansion of electromagnetic fields through interpolation

Marc Duruflé, Alexandre Gras, Philippe Lalanne

Improvement of the modal expansion of electromagnetic fields through interpolation

Marc Duruflé, Alexandre Gras, Philippe Lalanne

RESEARCH REPORT
N° 9382
December 2020
Project-Team Magique-3D

ISSN 0249-6399 ISRN INRIA/RR--9382--FR+ENG

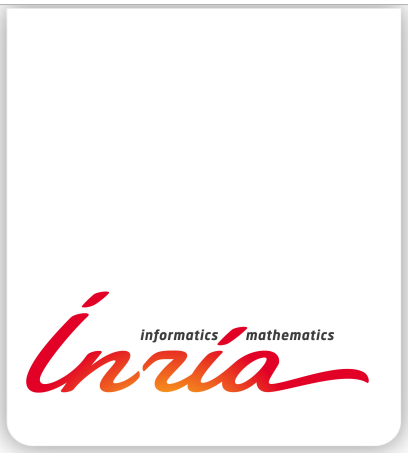

Improvement of the modal expansion of electromagnetic fields through interpolation

Marc Duruflé*, Alexandre Gras*†, Philippe Lalanne†

Project-Team Magique-3D

Research Report n° 9382 — December 2020 — 38 pages

Abstract: We consider optical structures where the dielectric permittivity is described as a rational function of the pulsation ω (Lorentz model). The electromagnetic fields can be computed on a large number of frequencies by computing the eigenmodes of the optical device and reconstructing the solution by expanding it on these eigenmodes. This modal expansion suffers from numerous limitations that are detailed in this report. In order to overcome these limitations, an interpolation procedure is proposed such that the direct computation of the electric field is needed only for a small number of interpolation points. Numerical experiments in 2-D and 3-D exhibit the efficiency of this approach.

Key-words: electromagnetic resonance, quasinormal mode, microcavity, nanoresonator, modal expansion

* Bordeaux INP, INRIA Bordeaux Sud-Ouest, EPI Magique 3-D
† LP2N, Institut d'Optique Graduate School, CNRS, Univ. Bordeaux

RESEARCH CENTRE
BORDEAUX – SUD-OUEST

200 avenue de la Vieille Tour
33405 Talence Cedex

Amélioration du développement modal des champs électromagnétiques par une méthode d'interpolation

Résumé : Nous considérons des structures optiques où la permittivité diélectrique est une fonction rationelle de ω (modèle de Lorentz). Les champs électromagnétiques peuvent être calculés pour un grand nombre de fréquences en calculant les modes propres du dispositif optique et en reconstruisant la solution en la développant sur ces modes. Ce développement modal souffre de nombreuses limitations qui sont détaillées dans ce rapport. Afin de dépasser ces limitations, une procédure d'interpolation est proposée de telle sorte que le champ électrique est calculé directement pour un petit nombre de points d'interpolation. Des expériences numériques en 2-D et 3-D montrent l'efficacité de cette approche.

Mots-clés : résonance électromagnétique, mode quasi-normal, microcavité, nano-résonateur, décomposition modale

Contents

1 Introduction **3**

2 General setting **4**

3 Limitations of the modal expansion **6**
3.1 Influence of the source term 6
3.1.1 Gaussian source 6
3.1.2 Incident plane wave 9
3.2 Dispersive materials 13
3.2.1 Germanium disk 13
3.2.2 Germanium sphere 16
3.3 Summary of limitations 17

4 Efficient Computation of eigenmodes **18**
4.1 Dispersive PMLs 18
4.2 Non-dispersive PMLs 19
4.3 Comparison of solvers 19

5 Interpolation procedure to reconstruct the field **21**
5.1 2-D cavity 22
5.2 3-D dolmen 27

6 Conclusion **30**

A Efficiency of interpolation on other cases **32**
A.1 2-D cobra cavity 32
A.2 3-D cobra cavity 33
A.3 Silica square 33
A.4 Germanium disk 34
A.5 Germanium sphere 36

B Displacement of roots and poles of the permittivity function **37**

1 Introduction

Optical micro- and nanoresonators localize and enhance the electromagnetic energy at wavelength and subwavelength scales and are a mainstay of many photonic devices. Their optical response is characterized by resonant features resulting from the excitation of one or a few dominant modes, intrinsic to the resonator. These modes of open, leaky resonator are oftentimes called quasinormal modes (QNMs) to emphasize that their harmonic evolution is characterized by an exponential damping in time, due to the non-Hermitian nature of the corresponding scattering operatorLalanne et al. (2018).

In order to compute the electric field for a wide range of frequencies, an approach consists of computing the modes characterizing the optical device, and expand the solution onto these modes :

$$\mathbf{E}(\mathbf{r},\omega) = \sum_m \alpha_m(\omega)\mathbf{E}_m(\mathbf{r},\omega),$$

where $\mathbf{E}_m$ is a mode, and $\alpha_m(\omega)$ the complex modal excitation coefficient. There exists different formulas for the coefficients α_m (see Lalanne et al. (2018) and Duruflé et al. (2020)). However, to reach a given accuracy, the number of modes used in the modal expansion can be very large (Yan et al. (2018), Duruflé et al. (2020)) whatever the used formula. We can cite the method developed in (Zimmerling et al., 2016) where the modes are computed simultaneously with the coefficients α_m such that only significant modes are kept in order to reduce this number of modes. Another approach described in (Binkowski et al., 2019; Zschiedrich et al., 2018) relies on an integration path in the complex frequency plane which encloses the eigenmodes of interests. The scattered field at the real frequency can thus be expressed as a sum of two contributions : a resonant contribution made up of contour integrals around the eigenfrequencies in the complex plane, and a non-resonant contribution, a setup that's echoed in (Colom et al., 2018).

In this report, we will try to explain why the number of modes can be very large, this is the object of the section 3. The limitations of the modal expansion (1) are sumarized in the sub-section 3.3. In order to overcome these limitations, we propose to interpolate the difference between the finite element solution and the modal solution. This difference is slowly varying such that a polynomial interpolation converges fastly. This process is described in section 5 with numerical results in 2-D and 3-D. In the section 4, we investigated different strategies to compute efficiently the eigenmodes $\mathbf{E}_m$ (see Demésy et al. (2020) on the same topic). In the appendix A, the interpolation procedure is tested in the cases detailed in section 3. The appendix B deals with the design of a permittivity function $\varepsilon(\omega)$ such that poles and roots are far from the real axis.

2 General setting

Our system is described by a permittivity distribution $\varepsilon(\mathbf{r},\omega)$. In this report, we consider a Padé approximant of this permittivity that respects the causality principle as detailed in (Sehmi et al., 2017) :

$$\varepsilon(\mathbf{r},\omega) = \begin{cases} \varepsilon_\infty + \displaystyle\sum_{d=1}^{D} \frac{i\eta_k}{\omega + i\tilde{\gamma}_k} + \sum_{k=1}^{L} \left(\frac{i\sigma_k}{\omega - \Omega_k} + \frac{i\bar{\sigma}_k}{\omega + \bar{\Omega}_k} \right), & \text{if } \mathbf{r} \in \Omega_{\text{res}} \\ \varepsilon_b \quad \text{otherwise} \end{cases} \tag{1}$$

where σ_k and Ω_k are complex coefficients and $\tilde{\gamma}_k, \eta_k$ are real coefficients. Ω_{res} is the domain of the resonator, ε_b is the background permittivity. In Duruflé et al. (2020), it is explained that the model (1) can be rewritten inside the resonator as

$$\varepsilon(\mathbf{r},\omega) = \varepsilon_\infty - \sum_{k=1}^{L} \frac{c_k - i\omega\sigma_k}{\omega^2 - \omega_{0,k}^2 + i\gamma_k\omega}, \tag{2}$$

with real coefficients $c_k,\ \sigma_k,\ \omega_{0,k}, \gamma_k$.

The electric field $\mathbf{E}_s$ solve the Maxwell's equations

$$-\omega^2\, \varepsilon(\mathbf{r},\omega)\, \mathbf{E}_s + \nabla \times \nabla \times \left(\mu^{-1}\mathbf{E}_s\right) = \mathbf{J}(\mathbf{r},\omega) \tag{3}$$

where $\mathbf{J}$ is a source term and μ the magnetic permeability. When the scattered field is computed, we take

$$\mathbf{J}(\mathbf{r},\omega) = \omega^2\, (\varepsilon(\mathbf{r},\omega) - \varepsilon_b)\, \mathbf{E}_{\text{inc}} \tag{4}$$

where ε_b is the background permittivity and $\mathbf{E}_{\text{inc}}$ the incident field. We will consider three different boundary conditions ($\mathbf{n}$ is the outgoing normale)

- Dirichlet condition : $\mathbf{E} \times \mathbf{n} = 0$
- Neumann condition : $(\nabla \times \mathbf{E}) \times \mathbf{n} = 0$
- Silver-Müller condition : $\dfrac{\mathbf{n}}{\mu} \times \mathrm{curl}(\mathbf{E}) = -i\omega\sqrt{\dfrac{\varepsilon}{\mu}}\,(\mathbf{n} \times (\mathbf{E} \times \mathbf{n}))$
  This last condition is also called first-order absorbing boundary condition. We note Γ_a the boundary where a Silver-Müller condition is set.

After discretization (e.g. with finite element method), $\mathbf{E}^{\mathrm{fem}}$ will solve the following linear system

$$-\omega^2\widetilde{\mathbf{M}}_h(\omega)\mathbf{E}^{\mathrm{fem}} - i\omega\widetilde{\mathbf{S}}_h(\omega)\mathbf{E}^{\mathrm{fem}} + \widetilde{\mathbf{K}}_h(\omega)\mathbf{E}^{\mathrm{fem}} = \widetilde{\mathbf{F}_h} \tag{5}$$

where $\widetilde{\mathbf{M}}_h(\omega)$ and $\widetilde{\mathbf{K}}_h(\omega)$ are matrices defined as

$$\left[\widetilde{\mathbf{M}}_h(\omega)\right]_{i,j} = \int_\Omega \varepsilon(\mathbf{r},\omega)\boldsymbol{\varphi}_j(\mathbf{r}) \cdot \boldsymbol{\varphi}_i(\mathbf{r})d\mathbf{r}$$

$$\left[\widetilde{\mathbf{S}}_h(\omega)\right]_{i,j} = \int_{\Gamma_a} \sqrt{\frac{\varepsilon}{\mu}}(\mathbf{n} \times \boldsymbol{\varphi}_j(\mathbf{r})) \cdot (\mathbf{n} \times \boldsymbol{\varphi}_i(\mathbf{r}))d\mathbf{r}$$

$$\left[\widetilde{\mathbf{K}}_h(\omega)\right]_{i,j} = \int_\Omega \frac{1}{\mu}\nabla \times \boldsymbol{\varphi}_j(\mathbf{r}) \cdot \nabla \times \boldsymbol{\varphi}_i(\mathbf{r})d\mathbf{r}$$

if edge elements are used (see Cohen and Duruflé (2007) for the expression of basis functions $\boldsymbol{\varphi}_i$). Ω is the computational domain. ε and μ are multiplied by a diagonal tensor in PML layers as explained in section 4.

The direct computation of $\mathbf{E}^{\mathrm{fem}}$ for N_f pulsations needs to solve N_f linear systems (5), which can be particularly costly if N_f is large. A popular approach consists of computing the discrete eigenvectors $\mathbf{E}_m$ that will solve

$$-\omega_m^2\widetilde{\mathbf{M}}_h(\omega_m)\mathbf{E}_m - i\omega_m\widetilde{\mathbf{S}}_h(\omega_m)\mathbf{E}_m + \widetilde{\mathbf{K}}_h(\omega_m)\mathbf{E}_m = 0$$

where ω_m is the eigenpulsation and of reconstructing the field $\mathbf{E}^{\mathrm{modal}}$ at the real frequency ω with these eigenmodes:

$$\mathbf{E}^{\mathrm{modal}}(\omega) = \sum_{m=1}^{N} \alpha_m(\omega)\mathbf{E}_m \tag{6}$$

where N is the number of modes used in the modal expansion. In this report, two different formulas will be considered :

$$\alpha_m = \frac{1}{i(\omega_m - \omega)} \int_{\Omega_{\mathrm{res}}} \mathbf{J}(\mathbf{r}) \cdot \mathbf{E}_m(\mathbf{r})d\mathbf{r} \tag{7}$$

or

$$\alpha_m = \frac{1}{i(\omega_m - \omega)} \int_{\Omega_{\mathrm{res}}} \frac{(\varepsilon(\mathbf{r},\omega_m) - \varepsilon_\infty(\mathbf{r}))}{(\varepsilon(\mathbf{r},\omega) - \varepsilon_\infty(\mathbf{r}))}\mathbf{J}(\mathbf{r}) \cdot \mathbf{E}_m(\mathbf{r})d\mathbf{r} \tag{8}$$

The last one provides most of the time better results (see Duruflé et al. (2020)). The modal solution $\mathbf{E}^{\mathrm{modal}}$ converges towards the finite element solution $\mathbf{E}^{\mathrm{fem}}$ as the number of modes N increases (see Yan et al. (2018), Duruflé et al. (2020)). However a great number of the discrete eigenmodes included in the expansion in those results bear no physical meaning. They are modes created from the use of Perfectly Matched Layers to bound the domain, oftentimes

labelled PML modes Yan et al. (2018); Vial et al. (2014); Lalanne et al. (2019), or other numerical modes spawned from the discretization of the continuous problem. While a resonant feature can usually be attributed to the excitation of a single mode, hundreds, if not thousands, of modes are necessary in order to converge towards the finite element solution. In that sense, few physical modes can qualitatively reconstruct the sharper variations of a spectrum while an amalgation of non-resonant physical modes Colom et al. (2018), PML modes and other numerical modes build a generally monotone, smooth function of the frequency.

3 Limitations of the modal expansion

In this section, dispersive PMLs are used such that eigenvalues are complex conjugate. The implementation of these PMLs is described in Duruflé et al. (2020). The formula (7) will be used to reconstruct the fields. The number of modes N that will be given is the number of stored modes such that $\mathrm{Re}(\omega_m) \geq 0$. The modes such that $\mathrm{Re}(\omega_m) < 0$ are not stored since they are obtained by conjugation. For all the cases presented in this section, we checked that if all the modes are included, the modal solution is equal to the finite element solution at machine precision.

3.1 Influence of the source term

The coefficients α_m depends on the source term $\mathbf{J}$. The modal solution can be very accurate with a limited number of modes if the source term is favorable. The tangential trace of quasinormal modes are continuous across the interface between the resonator and the background medium. As a result, it will be more favorable to have a continuous source term (at least the tangential trace).

3.1.1 Gaussian source

In this paragraph, we choose a gaussian source which is continuous:

$$\mathbf{J} = e^{\alpha|\mathbf{x}-\mathbf{x}_0|^2}\mathbf{u}$$

where $\mathbf{x}_0$ is the center of the gaussian, $\mathbf{u}$ its polarization. The coefficient α is given as

$$\alpha = -\frac{\log(10^{-6})}{r_0^2}$$

where r_0 is the radius of the gaussian. In the 2-D case, we take $\mathbf{u} = \mathbf{e}_z$ (TE mode), whereas in the 3-D case, we choose $\mathbf{u} = \mathbf{e}_x$.

2-D cobra cavity We consider a cobra cavity, with a first-order absorbing boundary condition on the right section and Dirichlet conditions on other boundaries. The height of the cavity is equal to 1μm and the width is equal to 5.732 μm. The indexes are uniform : $\varepsilon = \mu = 1$. This case has been chosen because it is almost a closed cavity (only a part of the boundary is open). For closed cavities, the modal expansion is especially efficient. The solution is displayed in figure 1 for two wavelengthes (500nm and 800nm) with $r_0 = 500$ nm. The eigenpulsations are plotted in figure 2 for $\mathrm{Re}(\omega) > 0$. Other pulsations can be obtained by symmetry with respect to axis Oy. For this case, the modal expansion works correctly. In table 1, we represent the relative L^2

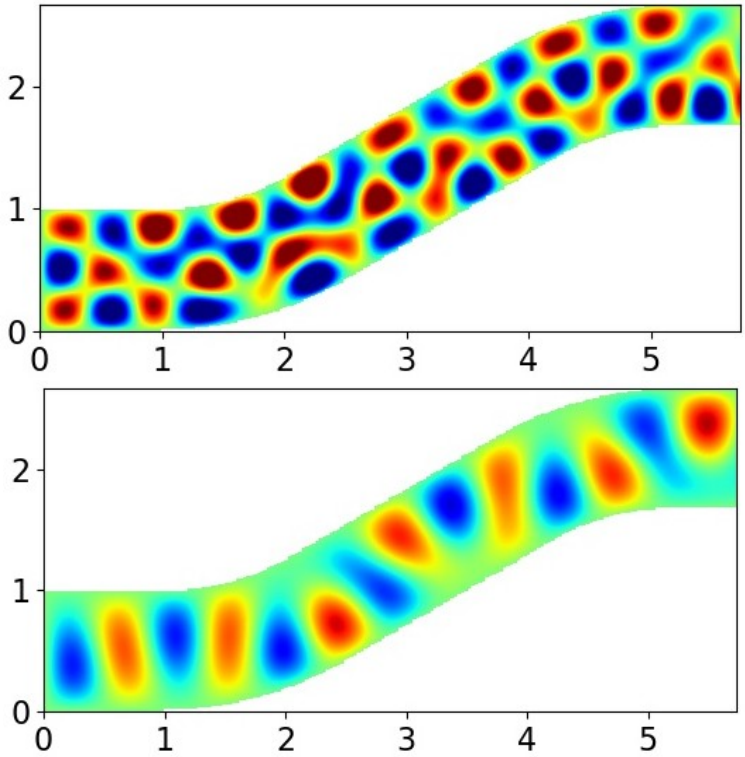

Figure 1: Real part of the solution for the 2-D cobra cavity for 500nm and 800nm

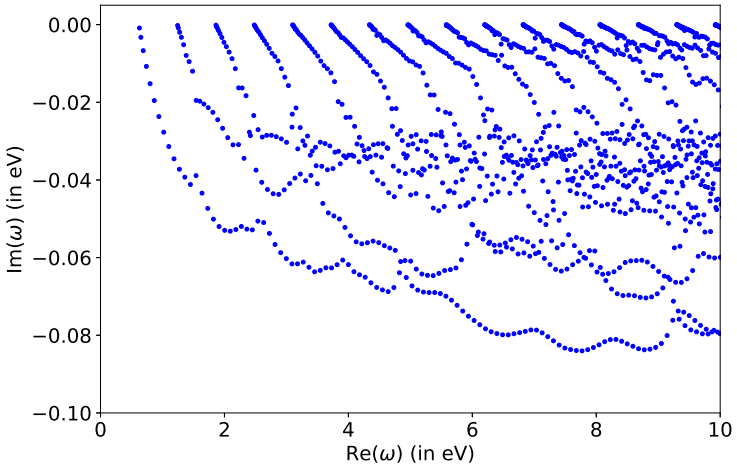

Figure 2: Spectrum for the 2-D cobra cavity

error between the modal solution and the finite element solution versus the number of modes N :

$$\text{Error} = \frac{\sqrt{\int_\Omega \left|\mathbf{E}^{\text{fem}} - \mathbf{E}^{\text{modal}}\right|^2 d\Omega}}{\sqrt{\int_\Omega \left|\mathbf{E}^{\text{fem}}\right|^2 d\Omega}}$$

This error is computed for 201 angular frequencies (between 1.24eV and 2.48eV which corresponds to wavelengthes between 500nm and 800nm) and we select the maximal error. We select modes

L (in eV)	1.97	2.96	3.95	4.93	5.92	6.91	7.89
N	39	91	174	272	406	558	732
Error (r_0=500nm)	1.0089	0.0671	0.01044	$2.572 \cdot 10^{-3}$	$4.796 \cdot 10^{-4}$	$9.934 \cdot 10^{-5}$	$1.4436 \cdot 10^{-5}$
Error (r_0=250nm)	1.0106	0.1027	0.03655	0.019143	0.009563	0.005576	0.00296

Table 1: Relative L^2 error for the 2-D cobra cavity.

such that $|\mathrm{Re}(\omega_m)| < L$, the values of L are also given in this table. We observe that by decreasing the radius r_0, the error will increase. The reason is that a narrower gaussian will excite more high-frequency modes. The numerical error obtained for the used mesh is below 10^{-5}. We observe that the modal expansion needs to compute the eigenpulsations until 7.89 eV to reach this error. This value is much larger than 2.48eV (the maximal frequency considered) and induces to compute a large number of modes to obtain a solution as accurate as the finite element solution.

3-D cobra cavity We have studied the 3-D cobra cavity in order to check that we had similar results in 3-D. We have imposed a Silver-Müller condition on the right section and perfect metal conditions ($\mathbf{E} \times \mathbf{n} = 0$) on other boundaries. The solution is given in figure 3 for 500nm. In

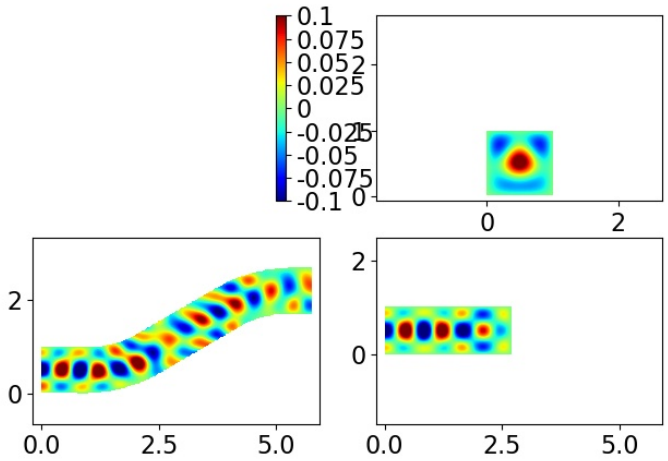

Figure 3: Real part of the solution for the 3-D cobra cavity for 500nm (component E_x of the electrical field).

figure 4, the numerical eigenpulsations are given. The relative L^2 error is computed for $\nabla \times \mathbf{E}$ in table 2. The mesh used for the computations provides a numerical error of 10^{-4}. We have similar conclusions to the 2-D case :

- the error increases for a narrower gaussian.
- to obtain an accurate solution, we need a very large number of modes

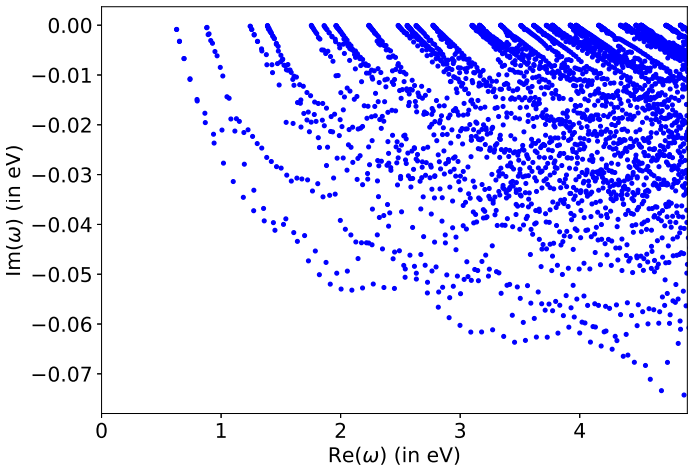

Figure 4: Spectrum for the 3-D cobra cavity

L	1.97	2.96	3.95	4.93
N	192	674	1611	3166
Error (r=500nm)	0.9986	0.09876	0.03070	0.01170
Error (r=250nm)	0.9989	0.2359	0.1553	0.1132

Table 2: Relative L^2 error for the 3-D cobra cavity.

Compared to the 2-D case, there are much more eigenpulsations, such that obtaining a modal solution as accurate as the finite element solution is out of reach.

3.1.2 Incident plane wave

1-D dielectric rod We consider a dielectric rod (interval $[-1,1]$) with $\varepsilon = 3$ inside the rod and $\varepsilon_b = 1$ outside (we choose $\varepsilon_0 = \mu_0 = c_0 = 1$). The computational domain is the interval $[-2,2]$. An absorbing condition (exact in 1-D) is set on the two extremities of the interval. We consider two types of sources

- Gaussian source $J = 3\, e^{-100(x-0.6)^2}$
- Incident plane wave $J = \begin{cases} 2e^{i\omega x} & \text{if } x \in [-1,1] \\ 0 & \text{otherwise} \end{cases}$

The gaussian source is regular such that it will be decomposed more efficiently into QNMs whereas the incident plane wave generates a discontinous source. Because of this discontinuity, it will excite much more QNMs. In figure 5, we display the magnitude of the excitation coefficient $\alpha_m(\omega)$ for the numerical eigenpulsations. We see clearly that for a gaussian, the highest eigenpulsations are not excited, whereas for an incident plane wave all the modes have a significant contribution. In figure 6, we displayed the magnitude of coefficients α_m for QNMs only. In 1-D, QNMs can be easily distinguished from ABC modes sinces their eigenpulsations are close to the real axis and are located on a same line (see figure 5). For a gaussian source, we observe an exponential

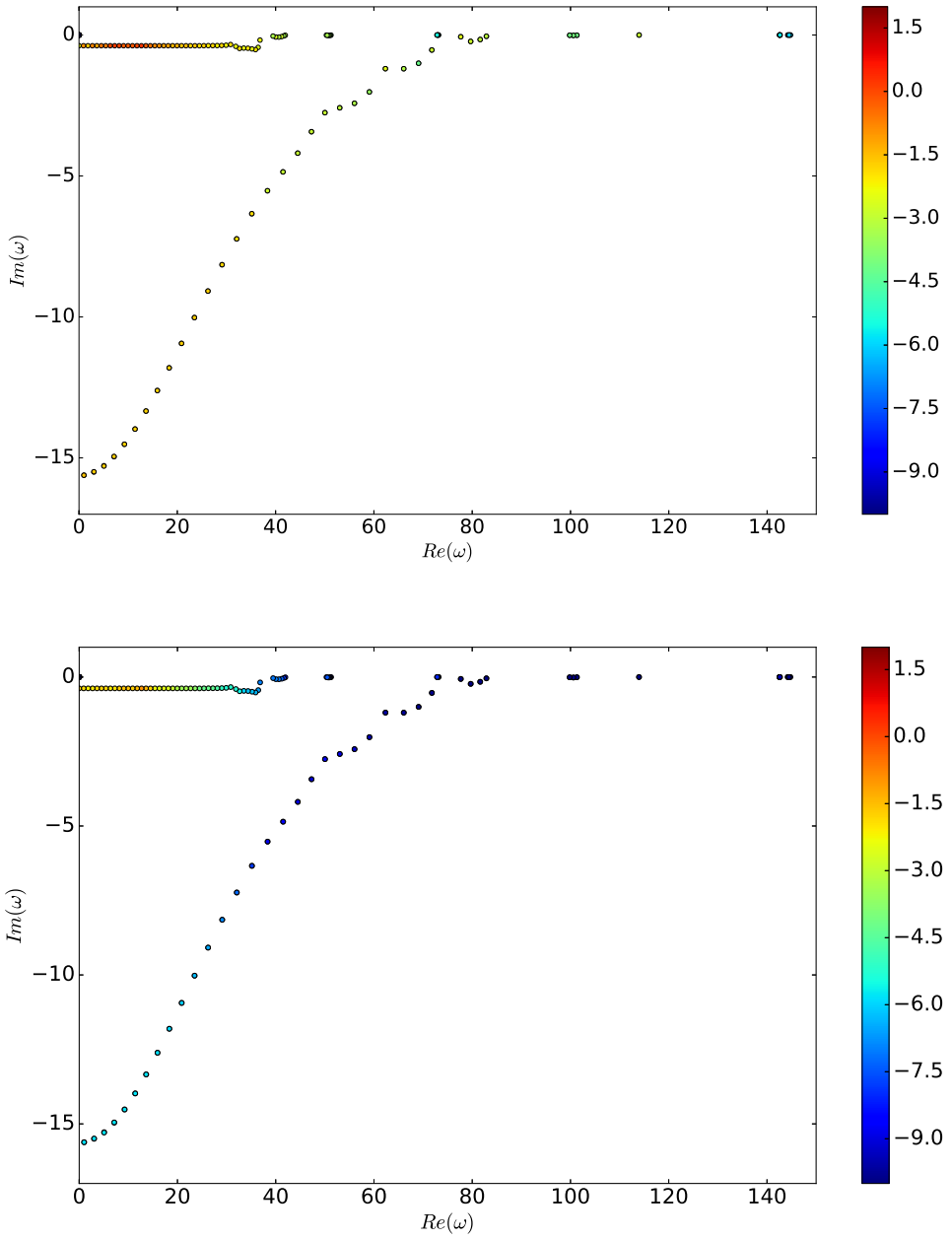

Figure 5: Eigenpulsations for a mesh size $h = 0.3$, the color of each point is given as $\log_{10}(|\alpha_j(\omega)|)$. On the top incident plane wave, on the bottom gaussian source.

decay of α_m versus m, whereas it decreases slowly for an incident plane wave. We relate this phenomenon to the Gibbs phenomenon, since we try to decompose a discontinous source into QNMs which are continuously derivable. It implies that the solution will exhibit high-frequency

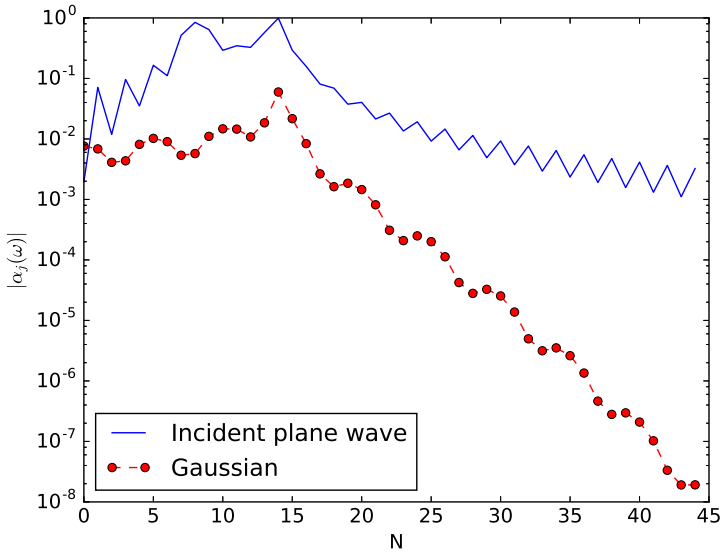

Figure 6: Modulus of α_m versus m for a gaussian source and incident plane wave with $\omega = 4\pi$.

oscillations close to the point of discontinuity (see figure 7).

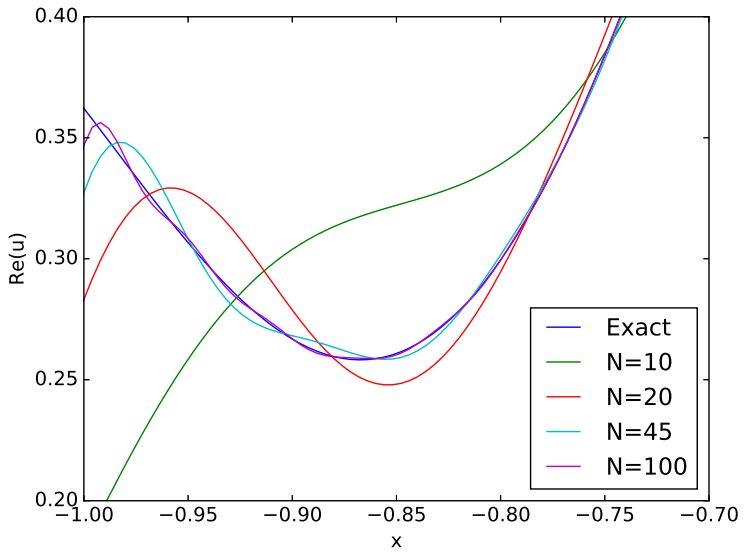

Figure 7: Real part of the solution (exact and modal solutions for different values of N). Case of an incident wave ($\omega = 4\pi$), the solution is represented on the interval $[-1, -0.7]$.

2-D dielectric square We consider a dielectric square with $\varepsilon = 2.25$ inside the resonator and $\varepsilon = 1$ outside. The squared resonator is 10 μm wide, the computational domain is 12 μm wide. PML layers are added to this computational domain, the thickness of these layers is set to 1 μm. The solution obtained for an incident plane wave with a wavelength of 2 μm is plotted in figure 8. The source is given by equation (4) with

$$\mathbf{E}_{\text{inc}}(x, y) = e^{i\frac{\omega x}{c_0}}$$

Similarly to the 1-D case, the modal solution oscillates close to the interface between the res-

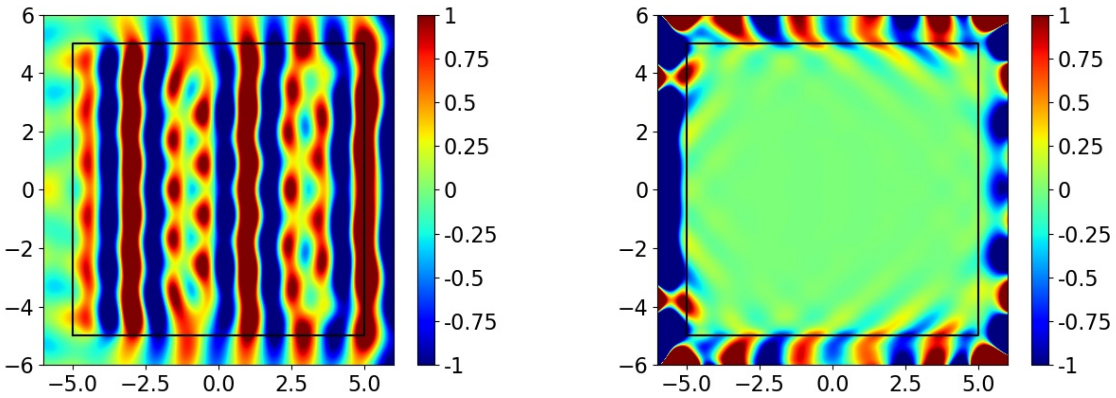

Figure 8: On the left, real part of the scattered field for a dielectric square ($\lambda = 2\mu m$). On the right, difference between the modal solution and the finite element solution.

onator and the background medium (right graph of figure 8). The modal solution has been obtained with dispersive PMLs with 3209 eigenmodes (and their complex conjugates). We computed eigenmodes close to the real axis, we obtained mainly QNMs (see figure 9). We compared

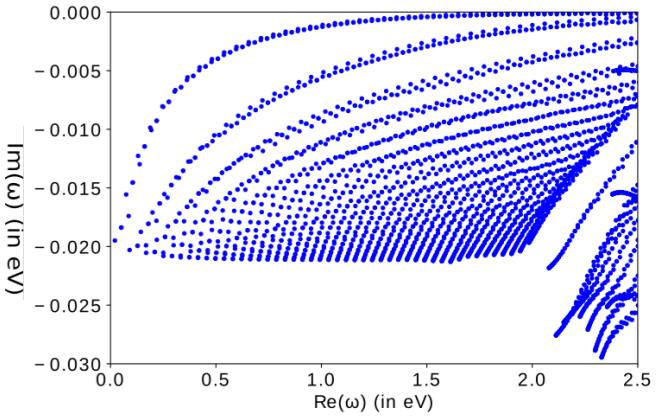

Figure 9: Numerical eigenpulsations for the dielectric square.

the accuracy obtained for two types of sources

- Gaussian source ($r_0 = 1.25\mu$m)
- Incident plane wave

N	784	1027	1969	3209
Plane wave	0.238644	0.137773	0.0859191	0.085545
Gaussian	0.155995	0.049234	0.020971	0.020966

Table 3: Relative L^2 error inside the resonator between the modal solution and the finite element solution versus the number od modes N. Case of the dielectric square.

We have computed the L^2 error inside the resonator for these two types of source (see table 3). We see that we obtain a better accuracy for the gaussian source as expected. For this case, we see also that increasing the number of modes does not necessarily improve the solution. For this case, with 1969 or 3209 modes, the accuracy is similar.

3.2 Dispersive materials

3.2.1 Germanium disk

We consider a disk of diameter 1 μm made of germanium surrounded by vacuum. The coefficients of the Lorentz model (with two poles) associated with this material are reproduced in table 4. These coefficients have been obtained by a least squares minimization over the interval

ε_∞	σ_1	Ω_1	σ_2	Ω_2
2.37031	10.767+12.8471i	2.22291-1.02029i	2.41218+0.64685i	2.07938-0.19684i

Table 4: Coefficients of the Lorentz model for the germanium (in electron-volts).

$[0.5, 2.5]eV$. In figure 10, we can check that this model is accurate in this interval. The field

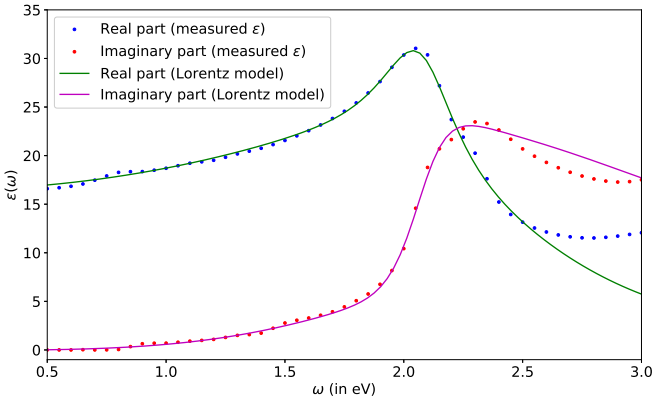

Figure 10: Dielectric permittivity $\varepsilon(\omega)$ for the germanium. Comparison between the measured permittivity and the Lorentz model with two poles.

driving the system is a plane wave propagating along the x-axis, at the real frequency ω. The

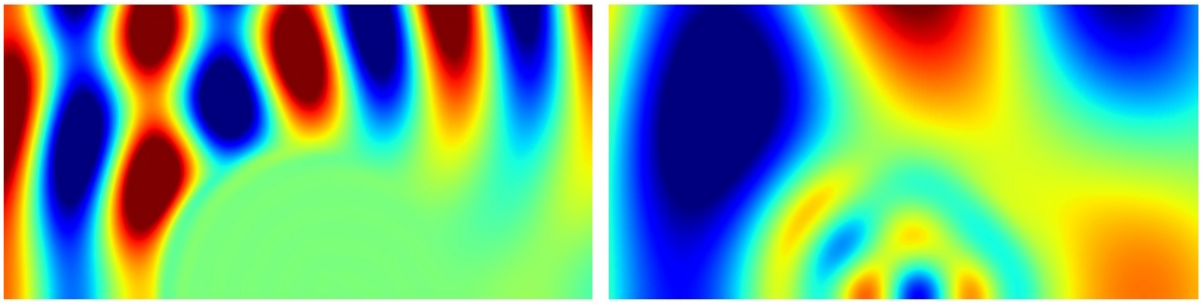

Figure 11: Real part of the total field for the germanium disk. On the left $\lambda = 500nm$, on the right $\lambda = 1.3\mu m$.

real part of the total field is plotted in figure 11 for two wavelengthes (500nm and 1.3μm). For short wavelengthes, the germanium behaves like a metal (with a strong damping) whereas it behaves like a dielectric for larger wavelengthes.

For a dispersive material, an interesting quantity is the complex wave number k defined as

$$k = \omega\sqrt{\varepsilon(\omega)\mu(\omega)}$$

In the figure 12, we have represented the imaginary part of this complex wave number in the complex plane when $\varepsilon(\omega)$ is governed by the Lorentz model (with coefficients of table 4). The

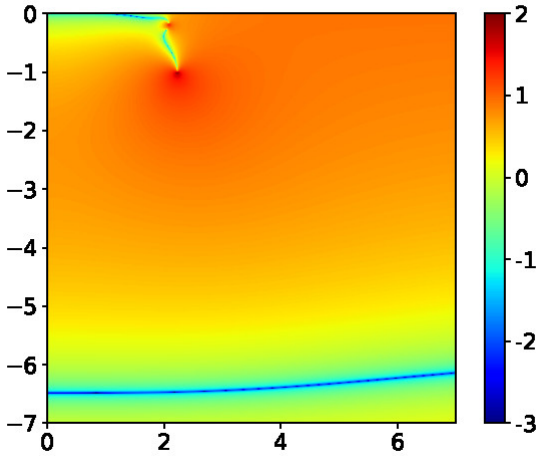

Figure 12: Imaginary part of complex wave number k in the complex plane

imaginary part of k represents the damping inside the material. For non-dispersive materials, the damping is small only close to the real axis. For non-dispersive materials, there are others regions with a small damping. In the case of the model used for the germanium, we have a small damping aroung $\mathrm{Im}(\omega) \approx -6.5eV$. The regions where we have a small damping are important since quasi-normal modes usually are located within these regions. In the figure 13, the numerical eigenpulsations ω_m are represented (blue dots). Eigenpulsations such that the complex wave

number $k_m = \omega_m \sqrt{\varepsilon(\omega_m)\mu_b}$ has an imaginary part greater than -1eV are symbolized with red squares. At this step, we can emphasize the following points

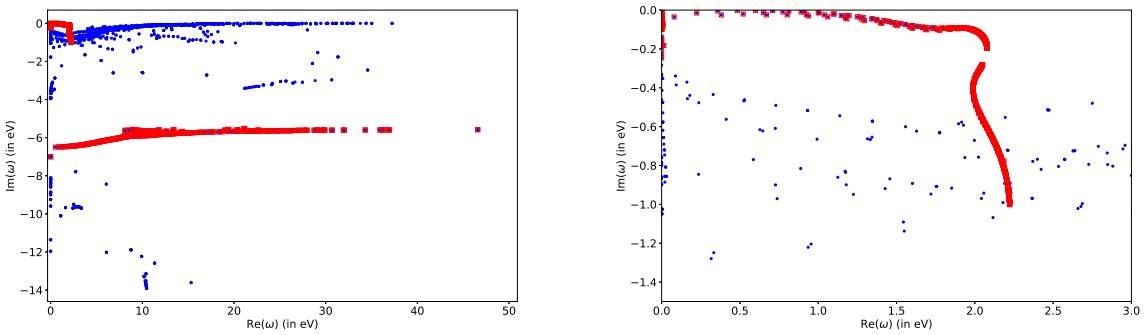

Figure 13: Spectrum for the germanium disk. On the right, zoom on a box. Red squares represent modes with a small imaginary part (in modulus) for the complex wave number k.

- Poles of $\varepsilon(\omega)$ are accumulation points, a lot of eigenvalues accumulate around these points. The number of eigenvalues is increasing (in $1/h^2$ where h is the mesh size) when the mesh is refined. Only a small part of these eigenvalues should be interesting (those with a small complex wave number).

- Regions such that the complex wave number has a small imaginary part contain interesting eigenvalues. However, these regions can be located in various parts of the complex plane, such that computing all the eigenmodes in these regions require several shifts. It is more complicated than in the non-dispersive case, where only eigenvalues close to the real axis are usually sought.

In figure 14, the error between the modal solution and the finite element solution is represented versus the pulsation ω. This error is computed only inside the disk. We select either eigenmodes close to the real axis ($\mathrm{Im}(\omega) > -1$) or eigenmodes with a complex wave number k with a small imaginary part ($\mathrm{Im}(k) > -1$). We see that the last criterion is more relevant than the second criterion, especially for pulsations where the material behaves as a metal. In table 5, the error

N	128	253	579	923	1885
Error	0.401953	0.298607	0.205992	0.175894	0.16374

Table 5: Relative L^2 error between the modal solution and the direct solution versus the number N of selected modes. Case of the germanium disk.

is computed for a different number of modes. The modes are selected by choosing $\mathrm{Im}(k) > -1$ and $\mathrm{Re}(k) < k_{\max}$. By selecting different values for $k_{\max}$, we obtain a different number of modes. The error is computed for 201 angular frequencies (between 500 nm and 1.3 μm) and the maximal error is retained. We see that the error decreases slowly, this is due to the source chosen (incident plane wave) as explained in the previous sub-section.

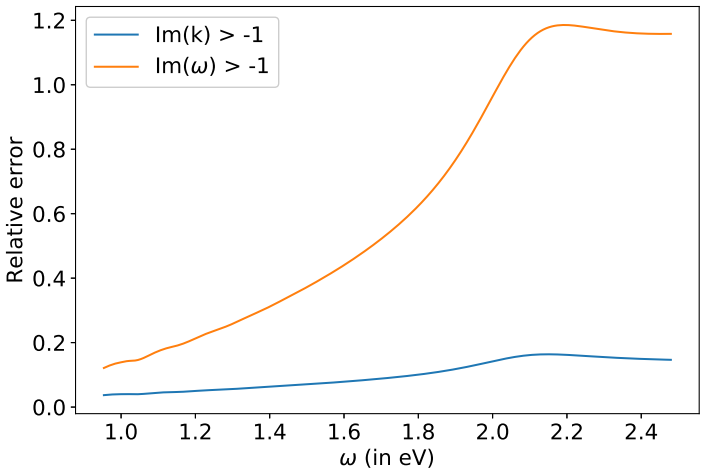

Figure 14: Relative L^2 error between the modal solution and the finite element solution versus the pulsation ω. Case of the germanium disk, eigenmodes such that $\mathrm{Im}(\omega) > -1$ or $\mathrm{Im}(k) > -1$ are selected.

3.2.2 Germanium sphere

We investigated the case of a sphere of radius 100nm made of germanium. The coefficients for the Lorentz model are the same as in the previous sub-section. The field driving the system is a plane wave, only a quarter of the sphere is meshed. With the used mesh and fourth-order edge elements a numerical error of 1% is obtained (compared to the analytical solution).

In table 6, we counted the number of eigenvalues close to poles or roots of $\varepsilon(\omega)$. The number of eigenvalues associated with static eigenmodes ($\omega_m = 0$) are also counted. In the case of roots

Order	1	2	3	4
Number of dofs	2002	7374	18426	37246
Number of eigenvalues located on roots	16	119	409	962
Number of eigenvalues close to poles	323	961	2174	4317
Number of static eigenvalues	941	2891	6285	11435

Table 6: Number of eigenvalues versus the order of approximation for the germanium sphere. Only eigenvalues such that $\mathrm{Re}(\omega_m) \geq 0$ are counted.

of $\varepsilon(\omega)$, the eigenvalues are accumulated very close to the root :

$$|\omega_m - z_k| < 10^{-6}$$

where z_k is a root of $\varepsilon(\omega)$. We see in table 6 that the number of eigenvalues located on roots grow linearly with respect to the number of dofs, but is much smaller than the number of static eigenvalues. In the case of poles of $\varepsilon(\omega)$, the eigenvalues are accumulated more progressively and constitute a path towards the pole (e.g. as illustrated in figure 13). We introduce the distance to the pole :

$$\mathrm{dist(pole)} = |\omega_m - \Omega_k|$$

where Ω_k is a pole of $\varepsilon(\omega)$. To establish the table 6, we have chosen a distance equal to 0.015. We observe that the number of eigenvalues close to the poles is much larger than eigenvalues close to the roots.

In table 7, we have computed the relative error for the curl of the electric field between the modal solution and the finite element solution. The error is computed for 201 angular frequencies

Criterion	N	Error
All eigenvalues	12 471	$2.44 \cdot 10^{-8}$
Eigenvalues in box $[0,40] \times [-6,0]$	11 768	$1.515 \cdot 10^{-4}$
Eigenvalues in box $[0,40] \times [-6,0]$, excluding eigenvalues on roots	10 806	$1.515 \cdot 10^{-4}$
Eigenvalues in box $[0,40] \times [-6,0]$, excluding eigenvalues on roots and poles with dist(pole) < 0.015	6480	$3.987 \cdot 10^{-3}$
Eigenvalues in box $[0,40] \times [-6,0]$, excluding eigenvalues on roots and poles with dist(pole) < 0.03	6207	$2.104 \cdot 10^{-2}$

Table 7: Number of eigenvalues satisfying a given criterion and associated relative L^2 error between curl $\left(\mathbf{E}^{\text{fem}}\right)$ amd curl $\left(\mathbf{E}^{\text{modal}}\right)$

(between 600 nm and 900 nm) and the maximal error is retained. We observe that excluding eigenvalues located on the roots of $\varepsilon(\omega)$ does not impact the accuracy. We can also exclude eigenvalues that are close enough to the poles. We see that the number of modes is divided by two by excluding eigenvalues associated with the accumulation points while the accuracy remains good.

3.3 Summary of limitations

In this subsection, we recapitulate the drawbacks of the reconstruction that have been illustrated previously :

1. Loss of accuracy : the modal solution can be much less accurate than the finite element solution. In order to obtain a similar accuracy, a very large number of modes can be needed.

2. Lack of robustness : the number of modes N needed to reach a given accuracy will depend strongly on the source $\mathbf{J}$. It can be very large for a discontinuous source (such as an incident plane wave) or a continuous source with a rapid variation (e.g. a narrow gaussian).

3. Lack of control : the error between the modal solution and the finite element solution can stagnate when N is increased. The convergence is rather slow especially for a discontinuous source.

4. Gibbs phenomenon : if only QNMs are included, the modal solution oscillates close to the interface between the resonator and the exterior domain in the case of a discontinuous source. The accuracy obtained on the interface is poor.

5. Loss of accuracy outside the resonator : in order to have an accurate solution outside the resonator, it may be necessary to include a large number of PML modes.

6. Need to compute eigenvalues in different parts of the complex plane :
   (a) In the non-dispersive case, we would like to compute only eigenvalues close to the interval $[\omega_1, \omega_2]$ on the real axis, since the solution will be reconstructed on this interval. However, it is actually necessary to compute modes on a larger zone with $Re(\omega) >> \omega_2$ due to Gibbs phenomenon.
   (b) In the case of dispersive materials, the complex wave number $\omega\sqrt{\varepsilon(\omega)\mu}$ can have a small imaginary part in different regions of the complex plane (depending on the locations of roots of $\varepsilon(\omega)$). To obtain an accurate modal solution, it is not sufficient to consider only eigenvalues close to the interval $[\omega_1, \omega_2]$ of the real axis.
7. Presence of accumulation points : for a dispersive material, poles and zeros of $\varepsilon(\omega)$ are accumulation points for the eigenvalues. In the case of a geometry with corners the solutions of $\varepsilon(\omega) = -1$ are also accumulation points. The number of eigenvalues near these points increases linearly with respect to the number of degrees of freedom. Most of the eigenmodes (especially when the eigenvalues are very close to the accumulation point) do not contribute significantly to the modal solution. However, the eigensolver can fail if the number of these eigenvalues is larger than the number of requested eigenvalues. These eigenvalues can also "hide" significant eigenvalues if the shift used to compute eigenvalues is not well located.

4 Efficient Computation of eigenmodes

In this section, we investigate different methods to compute efficiently eigenmodes. The aim is to select the best method in order to have an efficient reconstruction.

4.1 Dispersive PMLs

Dispersive PMLs consist of multiplying ε and μ by the following diagonal tensor

$$C(\omega) = \frac{(-i\omega + \mathbf{T}_{2,3,1})\,(-i\omega + \mathbf{T}_{3,1,2})}{-i\omega\,(-i\omega + \mathbf{T}_{1,2,3})}$$

where

$$\mathbf{T}_{i,j,k} = \begin{pmatrix} \sigma_i & 0 & 0 \\ 0 & \sigma_j & 0 \\ 0 & 0 & \sigma_k \end{pmatrix}$$

The damping coefficients σ_x, σ_y and σ_z inside a PML where $x > x_0$, $y > y_0$ or $z > z_0$ are parabolic:

$$\sigma_1 = \sigma_x = \frac{3\log(1000)}{2a^3}(x - x_0)^2 v_{max}\,\sigma$$

$$\sigma_2 = \sigma_y = \frac{3\log(1000)}{2a^3}(y - y_0)^2 v_{max}\,\sigma$$

$$\sigma_3 = \sigma_z = \frac{3\log(1000)}{2a^3}(z - z_0)^2 v_{max}\,\sigma.$$

The coefficient σ serves to adjust the reflection coefficient of the PML. v_{max} is the speed of the wave inside the PML and a is the thickness of PML layer. To implement, these PMLs, auxiliary fields are added such that the eigenvalue problem is linear :

$$\begin{cases} \text{Find } \omega_m \in \mathbb{C} \text{ and } \mathbf{U} \neq 0 \text{ such that} \\ -i\omega_m \mathbf{M}_h \mathbf{U} + \mathbf{K}_h \mathbf{U} = 0 \end{cases} \tag{9}$$

where the matrices $\mathbf{M}_h$ and $\mathbf{K}_h$ are real and do not depend on the eigenvalue value $\lambda_m = i\omega_m$. This process is detailed in (Duruflé et al., 2020). To solve the linear eigenvalue problem (9), we can use either Slepc or Arpack. For Arpack, we use the routine dneupd (for real matrices) with a complex shift. For Slepc, we use the solver EPS with complex numbers. A spectral transformation is used such that largest eigenvalues of $(\mathbf{K}_h - \sigma\mathbf{M}_h)^{-1}\mathbf{M}_h$ are sought to obtain the eigenvalues closest to the shift σ. In order to factorize the matrix $\mathbf{K}_h - \sigma\mathbf{M}_h$, the direct solver MUMPs is used (Amestoy et al. (2001)). A static condensation procedure (see chapter 3 of N'diaye (2017)) is performed in order to factorize a reduced linear system (auxiliary unknowns and internal degrees of freedom are removed). When Arpack is used, $2N$ eigenvalues are asked since the routine dneupd will compute complex conjugate eigenvalues. As a result N eigenvalues are obtained close to the shift σ and N eigenvalues are obtained close to $\bar{\sigma}$. When Slepc is used, N eigenvalues are asked since it will compute N eigenvalues close to the complex shift σ (without computing the eigenvalues close to $\bar{\sigma}$).

4.2 Non-dispersive PMLs

In the case of non-dispersive PMLs, ε and μ are multiplied by $C(\omega_0)$ where ω_0 is a given frequency usually chosen in the interval $[\omega_1, \omega_2]$ where the solution will be reconstructed. Maxwell's equations are written in the form

$$\begin{cases} -\omega^2 C(\omega_0)\left(\varepsilon_\infty \mathbf{E} + \sum_k \mathbf{P}_k\right) - \operatorname{curl}\left(\dfrac{1}{\mu_b C(\omega_0)}\operatorname{curl}\mathbf{E}\right) = 0 \\ -\omega^2 \mathbf{P}_k - i\omega\gamma_k \mathbf{P}_k + \omega_{0,k}^2 \mathbf{P}_k = c_k - i\omega\sigma_k \mathbf{E} \end{cases}$$

After discretization, we obtain a quadratic eigenvalue problem

$$\begin{cases} \text{Find } \omega_m \in \mathbb{C} \text{ and } \mathbf{U} \neq 0 \text{ such that} \\ -\omega_m^2 \mathbf{M}_h \mathbf{U} - i\omega_m \mathbf{S}_h \mathbf{U} + \mathbf{K}_h \mathbf{U} = 0 \end{cases} \tag{10}$$

where $\mathbf{M}_h, \mathbf{S}_h$ and $\mathbf{K}_h$ are complex matrices. To solve this polynomial eigenvalue problem, we use PEP solver proposed in Slepc. As described in Campos and Roman (2016), a spectral transformation is used such that largest eigenvalues θ of the quadratic eigenvalue problem

$$\theta^2\left(\mathbf{K}_h - \sigma\mathbf{S}_h - \sigma^2\mathbf{M}_h\right)\mathbf{x} - \theta\left(\mathbf{S}_h + 2\sigma\mathbf{M}_h\right)\mathbf{x} - \mathbf{M}_h\mathbf{x} = 0$$

are sought, and eigenvalues $\lambda_m = i\omega_m$ closest to the shift σ are obtained as

$$\lambda_m = \sigma + \frac{1}{\theta}$$

The matrix $\left(\mathbf{K}_h - \sigma\mathbf{S}_h - \sigma^2\mathbf{M}_h\right)$ is factorized with Mumps. A static condensation procedure is also used in order to factorize a reduced linear system. For both cases (dispersive or non-dispersive PMLs), this linear system has the same size.

4.3 Comparison of solvers

We compare the following solvers

- Dispersive PMLs + Arpack
- Dispersive PMLs + Slepc

Solver	Time (one core)	Time (8 cores)	# Linear solves
Dispersive + Arpack	13.2s	3.3s	322
Dispersive + Slepc	8.5s	2.3s	215
Non-dispersive	5.3s	1.8s	213

Table 8: Computation time (and number of linear solves) needed to compute 80 modes for the 2-D cobra cavity (11 111 degrees of freedom).

Solver	Time (8 cores)	Time (16 cores)	# Linear solves
Dispersive + Arpack	411s	311s	602
Dispersive + Slepc	274s	198s	384
Non-dispersive	248s	177s	384

Table 9: Computation time (and number of linear solves) needed to compute 120 modes for the 3-D cobra cavity (467 509 degrees of freedom).

- Non-dispersive PMLs (only Slepc is considered)

This comparison is conducted for the cases detailed in section 3. The results are given in the tables 8, 9, 10 and 11. The number of degrees of freedom given in these tables refer to the number of degrees of freedom for the unknown $\mathbf{E}$ only. For all these solvers, the computation is performed with a spectral transformation as detailed above. The coefficient σ is the shift such that the eigenvalues closest to σ are retrieved. Only one shift is used to obtain the eigenmodes in this section. In these tables, we count the number of linear solves. For example, in the dispersive case, the matrix $(\mathbf{K}_h - \sigma\mathbf{M}_h)$ is factorized once for the chosen shift σ and we count the number of linear solves. The computations can be computed in sequential (one core) or in parallel (the number of cores is provided). In these results, we observe that the solver Dispersive + Arpack is

Solver	Time (one core)	Time (8 cores)	# Linear solves
Dispersive + Arpack	46.9s	15.1s	702
Dispersive + Slepc	27.4s	9.4s	448
Non-dispersive	21.5s	10.3s	623

Table 10: Computation time (and number of linear solves) needed to compute 100 modes for the germanium disc (5 131 degrees of freedom).

Solver	Time (one core)	Time (8 cores)	# Linear solves
Dispersive + Arpack	66.4s	19.9s	314
Dispersive + Slepc	38.2s	11.5s	175
Non-dispersive	57.5s	20.1s	394

Table 11: Computation time (and number of linear solves) needed to compute 20 modes for the germanium sphere (46 672 degrees of freedom).

less efficient. Non-dispersive PMLs are most of the time more efficient than the solver Dispersive

+ Slepc. But it may occur (cf. table 11) that the solver Dispersive + Slepc requires much less iterations inducing a smaller computation time.

5 Interpolation procedure to reconstruct the field

In this section, we propose an interpolation strategy in order to overcome the encountered limitations in section 3. We denote $\mathbf{u}(\mathbf{r},\omega)$ the difference between the finite element solution and the modal expansion:

$$\mathbf{u}(\mathbf{r},\omega) = \mathbf{E}^{\text{fem}}(\mathbf{r},\omega) - \mathbf{E}^{\text{modal}}(\mathbf{r},\omega) = \mathbf{E}^{\text{fem}}(\mathbf{r},\omega) - \sum_{m=1}^{N} \alpha_m(\omega)\mathbf{E}_m(\mathbf{r}). \tag{11}$$

We consider real frequencies ω within the range $[\omega_1,\omega_2]$. If we include N eigenmodes such that all the resonances within the spectra are accounted for, then the difference $\mathbf{u}(\mathbf{r},\omega)$ is a slowly varying function within $[\omega_1,\omega_2]$. It can thus be conveniently approximated by a polynomial in ω.

We choose N_i interpolation points scattered within $[\omega_1,\omega_2]$:

$$\widetilde{\omega}_k = \omega_1 + x_k(\omega_2-\omega_1), \tag{12}$$

where x_k are points over the interval $[0,1]$. Many set of interpolation points can be used for an efficient interpolation, we have investigated three families of points:

- Chebyshev points: $x_k = \frac{1}{2} + \frac{1}{2}\cos\left(\frac{2k-1}{2N_i}\pi\right)$, $k = 1..N_i$
- Clenshaw-Curtis points: $x_k = \frac{1}{2} + \frac{1}{2}\cos\left(\frac{k-1}{N_i-1}\pi\right)$, $k = 1..N_i$
- Leja points defined recursively as (see P. Jantsch (2016)):

$$x_k = \text{argmax}_{x\in[0,1]} \prod_{i=1}^{k-1} |x - x_i|,\ k > 1$$

  with $x_1 = \frac{1}{2}$.

All these points avoid the Runge phemonemom such that the interpolation of a smooth function will converge exponentially. Leja points have the advantage to constitute a nested sequence of points, these points are reproduced in table 12. For the other points, there exists a nested sequence with $N_i = 1,3,9,27,\cdots$ for Chebyshev, and $N_i = 1,3,5,9,17,33,\cdots$ for Clenshaw-Curtis points. $\mathbf{u}(\mathbf{r},\omega)$ can be approximated by the following polynomial:

$$\mathbf{u}(\mathbf{r},\omega) \approx \sum_{k=1}^{N_i} \mathbf{u}_k\,\varphi_k(\omega), \tag{13}$$

with $\mathbf{u}_k = \mathbf{u}(\omega_k)$ and $\varphi_k(\omega) = \dfrac{\prod_{j=1,j\neq k}^{N_i} \omega - \widetilde{\omega}_j}{\prod_{j=1,j\neq k}^{N_i} \widetilde{\omega}_k - \widetilde{\omega}_j}$. The scattered field can thus be approximated as :

$$\mathbf{E}_s^I = \sum_{m=1}^{N} \alpha_m(\omega)\widetilde{\mathbf{E}}_m(\mathbf{r}) + \sum_{k=1}^{N_i} \mathbf{u}_k\,\varphi_k(\omega). \tag{14}$$

x_1	x_2	x_3	x_4	x_5	x_6	x_7	x_8
0.5	0	1	0.2113248	0.8293532	0.0803729	0.9350035	0.6528066

x_9	x_{10}	x_{11}	x_{12}	x_{13}	x_{14}
0.3391461	0.0285104	0.9763366	0.7397061	0.1436806	0.4220203

x_{15}	x_{16}	x_{17}	x_{18}	x_{19}	x_{20}	x_{21}
0.8874361	0.0102611	0.5805826	0.9916631	0.26931469	0.0540535	0.7859485

Table 12: Leja points x_i (until $i = 21$). Only seven first digits are reproduced.

We can observe that any formula for α_m (e.g. given by the equation (7) or (8)) can be written as

$$\alpha_m(\omega) = \frac{1}{i(\omega_m - \omega)} \int_\Omega \mathbf{J}(\omega_m) \cdot \mathbf{E}_m dx + \beta_0 + \beta_1(\omega - \omega_m) + \beta_2(\omega - \omega_m)^2 + \cdots$$

In this expression, the first term is a singular part (equal to the residue of $\alpha_m(\omega)$ divided by $\omega_m - \omega$) whereas other terms constitute a regular part. The different formulas for α_m have the same singular part but the regular part (coefficients β_i) will differ. As a result, we numerically observe that the convergence of $\mathbf{E}_s^I$ towards the finite element solution $\mathbf{E}^{\text{fem}}$ almost does not depend on the chosen formula for α_m. In this section, we will use the formula (8), but the results are very similar with other formulas.

5.1 2-D cavity

We consider the case of a 2-D cavity with two rows of circular holes (see figure 15) placed in an hexagonal pattern. The big circles have a radius of 40 nm while the small circles have a radius of 28 nm. The hole distance a is equal to 120nm, the small circles have been displaced by

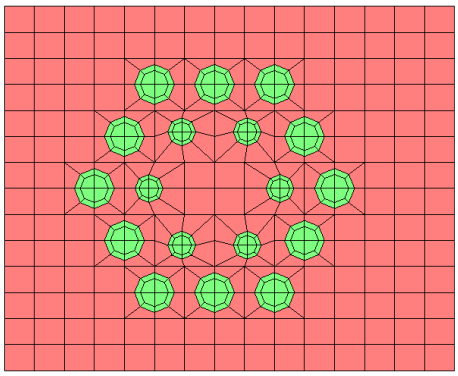

Figure 15: Mesh used for the 2-D cavity

$0.09a$ in radial direction. The holes are made of silicon, which is modeled as a Lorentz material with coefficients of table 13 (Eq. (1) with $D = 0$). The background medium has a constant

permittivity $\varepsilon_b = 4$. The field driving the system is a plane wave propagating along the x-axis,

Table 13: Constants ε_∞, σ_k, Ω_k for silicon. σ_1 and Ω_1 are given in electron-volts.

ε_∞	σ_1	Ω_1
1.12648273	2.17595+20.77585i	3.95095-0.190893i

at the real frequency ω : $\mathbf{E}_{\text{inc}} = e^{ikx}\mathbf{e}_z$ where $k = \dfrac{\omega}{c_0}$ is the wave number. The field is computed

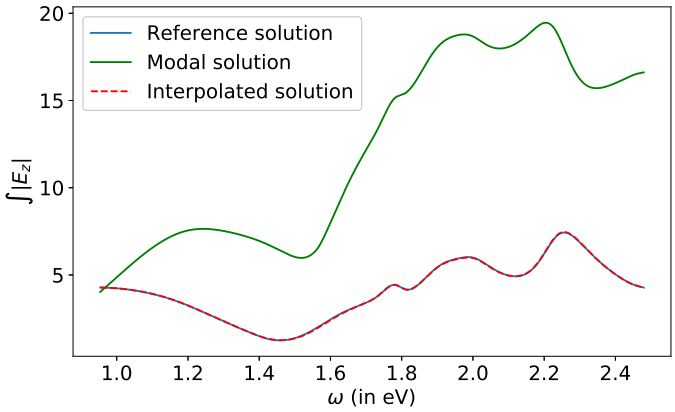

Figure 16: Mean value of $|E_z|$ at the right extremity of the mesh for the reference solution, the modal solution and the interpolated one.

for 401 angular frequencies ω evenly spaced in the interval $[\omega_1, \omega_2]$ where

$$\omega_1 = \frac{2\pi c_0}{\lambda_1}, \quad \omega_2 = \frac{2\pi c_0}{\lambda_2}.$$

The two wavelengthes λ_1, λ_2 are equal to 1.3 μm and 500 nm. It corresponds to $\omega_1 \approx 0.954eV$, $\omega_2 \approx 2.48eV$. We use sixth-order finite element method with the mesh of figure 15, PML layers are added around this mesh. The numerical error is around 10^{-5} for this mesh. In figure 16, we display the mean value of $|\mathbf{E}_z|$ (scattered field) for $x = 420nm$. We see that the modal solution and the reference solution have peaks located at the same positions. However, they are very different mainly because the number of modes used in the modal expansion is limited. The modal solution has been computed with only 100 modes and non-dispersive PMLs. The eigenpulsations ω_m of these modes are displayed in figure 17. The mode associated with the eigenpulsation $1.78366 - 0.042718i$ (in eV) is plotted in figure 18. In figure 19, the reference solution and the modal solution are represented for λ =500nm. We see that they differ greatly outside of the silicon discs. In figure 20 the difference between the modal solution and the reference solution is represented for the point $(199.5nm, 0)$. It is observed that this difference is slowly varying and can be interpolated efficiently with a small number of points. In figure 21, the relative L^2 error is computed between the reference solution and the interpolated solution for different sets of points. This error is computed on all the physical domain (PML layers are excluded). For this case, the different interpolation points provide a similar accuracy. Only seven points are sufficient to obtain a solution quite accurate. These seven interpolation points have been used for the figure 16 (Clenshaw-Curtis points). Regarding the computation time, the interpolation

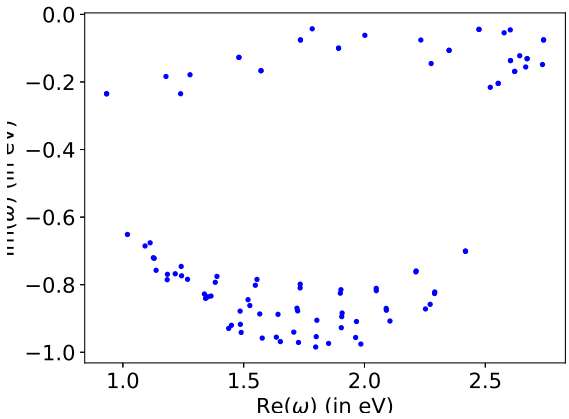

Figure 17: Eigenpulsations ω_m computed numerically for the 2-D cavity.

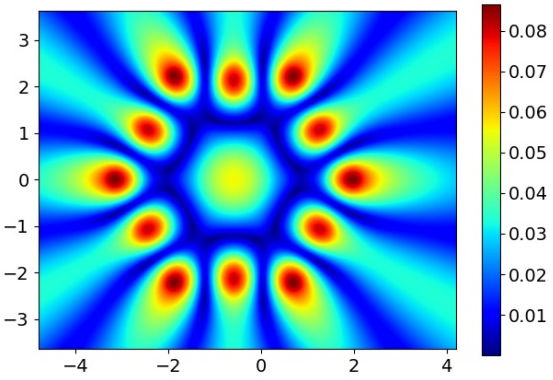

Figure 18: Modulus $|E_z|$ of the QNM associated with the eigenpulsation $1.78372211-0.04271975i$.

procedure with sevent points provides the solution in 27s for 401 angular frequencies. A direct computation (by factorizing and solving 401 linear systems) needs 85s. The computations have been launched on two cores.

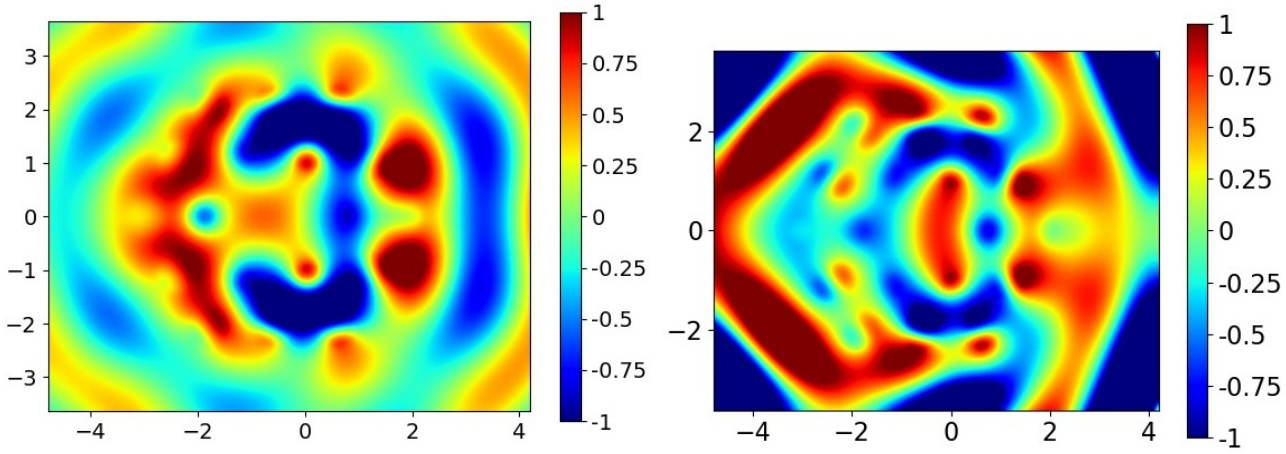

Figure 19: On the left, real part of the finite element solution, on the right real part of the modal solution. Case of the 2-D cavity with $\lambda = 500$ nm.

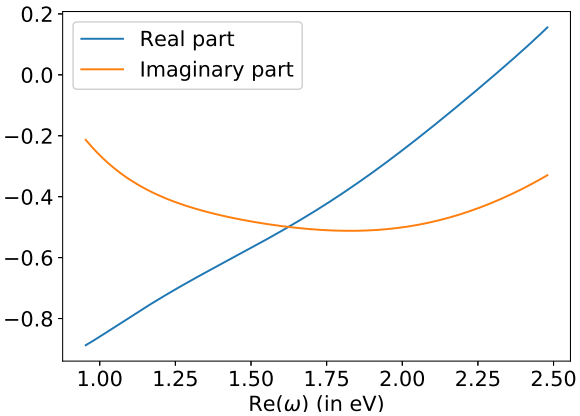

Figure 20: Difference between the reference solution and the modal solution for the 2-D cavity. Real part and imaginary part of this difference are computed at $(x, y) = (199.5nm, 0)$.

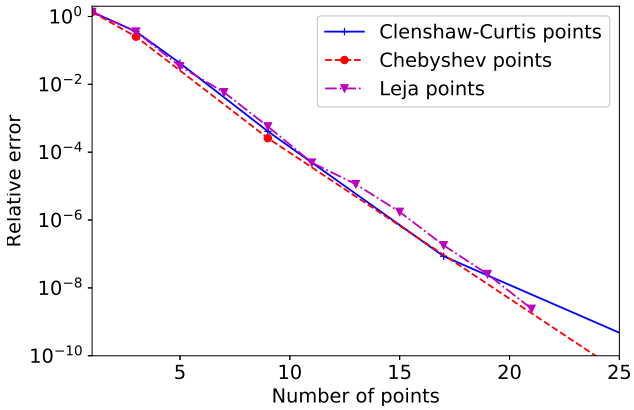

Figure 21: Relative L^2 error between the reference solution and the interpolation solution versus the number of interpolation points. Case of the 2-D cavity.

5.2 3-D dolmen

We consider the scattering of a dolmen-shaped resonator of dimensions 300 nm x 200 nm x

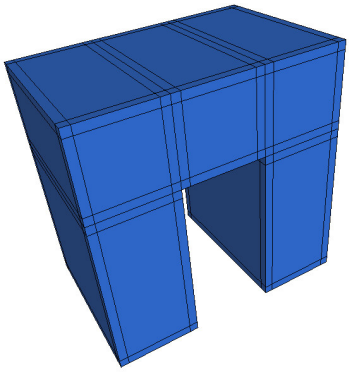

Figure 22: Surface mesh of the dolmen-shaped resonator

300nm. The internal cavity is a box of dimensions 100nm x 200 nm x 200 nm. The surface mesh of the resonator is displayed in figure 22, it is refined close to edges and corners to capture correctly singularities of the scattered field. The interior of the dolmen is made of silver which is

Table 14: Constants ε_∞, γ, σ, σ_k, Ω_k for silver.

ε_∞	σ	γ	σ_1
1.2135	883.46	0.0866887	3.5366 + 4.5884i

Ω_1	σ_2	Ω_2
4.249 - 2.1153i	0.74248e - 0.19950i	4.0097 - 0.30102i

represented by a Drude-Lorentz material with coefficients given in table 14 while the exterior is the vacuum ($\varepsilon_b = 1$). The incident field is a plane wave polarized at 30°, the solution is plotted in figure 23 for a wavelength of 400nm. The electric field is computed for 301 angular frequencies

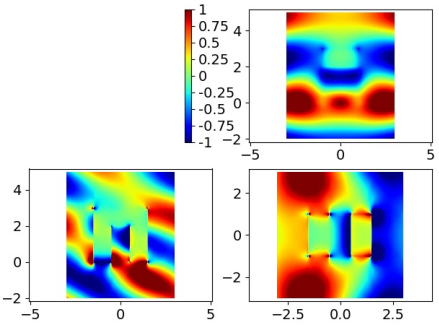

Figure 23: Real of the total field (component E_x) for $\lambda = 400nm$.

ω evenly spaced in the interval $[\omega_1, \omega_2]$ where

$$\omega_1 = \frac{2\pi c_0}{\lambda_1}, \quad \omega_2 = \frac{2\pi c_0}{\lambda_2}.$$

The two wavelengthes λ_1, λ_2 are equal to 800 nm and 400 nm. It corresponds to $\omega_1 \approx 1.55eV$, $\omega_2 \approx 3.10eV$. We use fourth-order edge finite element method. The numerical error is around 5% for the mesh used. In figure 24, we display the magnitude of the scattered field $||E_S||$ for a point

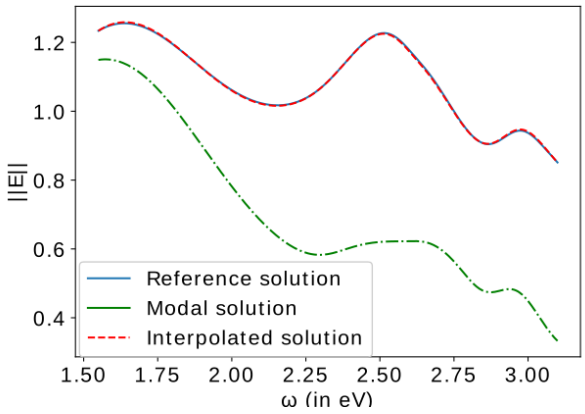

Figure 24: $||E_S||$ at a point located above the dolmen for the reference solution, the modal solution and the interpolated one.

located above the dolmen. We see that the modal solution and the reference solution have peaks located at the same positions. However, they are very different mainly because the number of modes used in the modal expansion is limited. The modal solution has been computed with only 80 modes with dispersive PMLs (Dispersive PML + Slepc solver). The eigenpulsations ω_m of these modes are displayed in figure 25. In figure 26 the difference between the modal solution

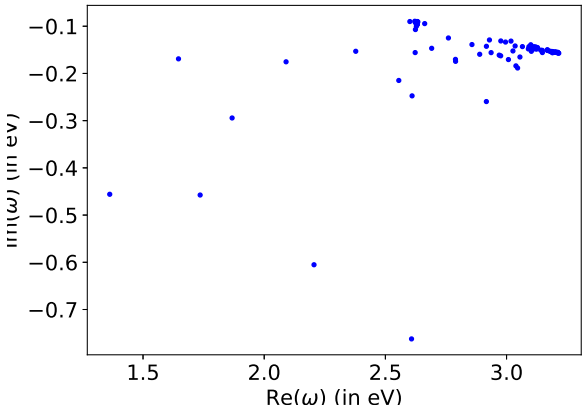

Figure 25: Eigenpulsations ω_m computed numerically for the dolmen.

and the reference solution is represented for the same point. It is observed that this difference

is slowly varying and can be interpolated efficiently with a small number of points. In figure 27,

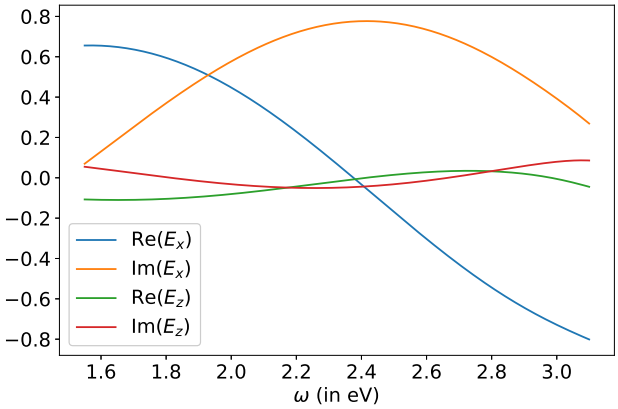

Figure 26: Difference between the reference solution and the modal solution for the dolmen. For the selected point, we have a null y-component of the electric field.

the relative L^2 error is computed between the reference solution and the interpolated solution for different sets of points. This error is computed on all the physical domain (PML layers are excluded). For this case, the different interpolation points provide a similar accuracy. Only five points are sufficient to obtain a solution quite accurate. These five interpolation points have been used for the figure 24 (Leja points). The interpolation procedure with these five points provides a

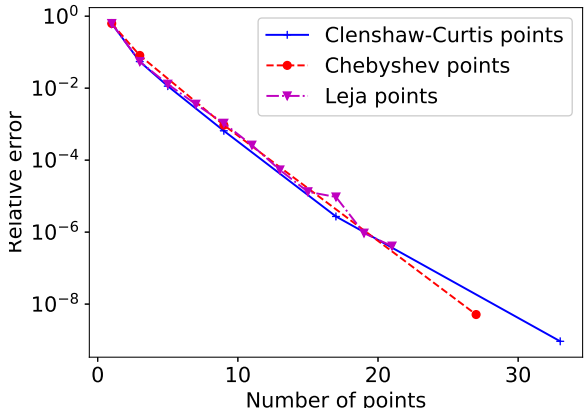

Figure 27: Relative L^2 error between the reference solution and the interpolation solution versus the number of interpolation points N. Case of the dolmen.

solution in 671s (301 frequencies) whereas a direct computation needs 11209s. The computations have been launched on 16 cores. In order to handle accumulation points, we propose an approach in appendix B such that poles and roots of ε are better located.

6 Conclusion

In section 3, we have detailed and illustrated the drawbacks of reconstructing the solution on a given interval $[\omega_1, \omega_2]$ by using the eigenmodes of the optical device. Because of these drawbacks, the reconstruction is often inefficient in comparison to a direct computation. We have proposed in section 5 an interpolation procedure to overcome these limitations. This strategy is based on the interpolation of the difference between the modal solution and the finite element solution. If eigenmodes close to the interval $[\omega_1, \omega_2]$ on the real axis are included, this difference is slowly varying and can be interpolated efficiently with a few number of points. By using a nested sequence of interpolation points such as Leja points, we can stop the computation as soon as the solution is accurate enough. With this approach, we obtain the following nice properties that solve the limitations listed in paragraph 3.3:

- Accuracy : the accuracy can be quickly improved by adding a few interpolation points. We no longer need to include a very large number of modes in order to improve the accuracy.
- Robustness : the convergence is fast and almost does not depend on the source term $\mathbf{J}$. The convergence depends mainly on the set of eigenpulsations included in the modal expansion.
- Control : we can reach a given accuracy by increasing the number of interpolation points.
- Accuracy outside the resonator : the accuracy is very good outside the resonator, we do not need to include a larger number of PML modes.
- Eigenvalues in a limited region of the complex plane : Only eigenvalues close to the interval $[\omega_1, \omega_2]$ on the real axis are needed.
- Accumulation points : the interpolation procedure itself does not solve this issue. Since the permittivity is not null, neither infinite, nor equal to -1 (except for metamaterials) on the real axis, it seems possible to obtain an analytic approximation of $\varepsilon(\omega)$ such that poles and zeros are far enough from the real axis. In appendix B, an attempt is made in order to take these accumulation points away from the real axis.
- Independence from the chosen formula for α_m : the convergence is similar with the different formulas for α_m (e.g. formulas (7), (8)). Moreover, the electric field can be reconstructed in 3-D directly with these formulas without the necessity of including static modes.

Finally numerical results presented in section 5 and in appendix A show that the interpolation procedure is computationally efficient.

References

Amestoy, P., Duff, I., Koster, J., and L'Excellent, J.-Y. (2001). A fully asynchronous multifrontal solver using distributed dynamic scheduling. SIAM Journal on Matrix Analysis and Applications, 23:15–41.

Binkowski, F., Zschiedrich, L., and Burger, S. (2019). An auxiliary field approach for computing optical resonances in dispersive media. J. Eur. Opt. Soc.-Rapid Publ.

Campos, C. and Roman, J. E. (2016). Parallel Krylov solvers for the polynomial eigenvalue problem in SLEPc. SIAM Journal on Scientific Computing, 38(5):385–411.

Cohen, G. and Duruflé, M. (2007). Non spurious spectral-like element methods for Maxwell's equations. Journal of Computational Mathematics, 25:282–304.

Colom, R., Mcphedran, R., Stout, B., and Bonod, N. (2018). Modal expansion of the scattered field: Causality, nondivergence, and nonresonant contribution. Physical Review B : Condensed matter and materials physics, 98:085418.

Demésy, G., Nicolet, A., Gralak, B., Geuzaine, C., Campos, C., and Roman, J. E. (2020). Non-linear eigenvalue problems with GetDP and SLEPc: Eigenmode computations of frequency-dispersive photonic open structures. Computer Physics Communications, 257:107509.

Duruflé, M., Gras, A., and Lalanne, P. (2020). Non-uniqueness of the quasinormal mode expansion of electromagnetic Lorentz dispersive materials. Technical Report RR-9348, INRIA.

Lalanne, P., Yan, W., Gras, A., Sauvan, C., Hugonin, J.-P., Besbes, M., Demésy, G., Truong, M. D., Gralak, B., Zolla, F., Nicolet, A., Binkowski, F., Zschiedrich, L., Burger, S., Zimmerling, J., Remis, R., Urbach, P., Liu, H. T., and Weiss, T. (2019). Quasinormal mode solvers for resonators with dispersive materials. J. Opt. Soc. Am. A, 36(4):686–704.

Lalanne, P., Yan, W., Vynck, K., Sauvan, C., and Hugonin, J.-P. (2018). Light interaction with photonic and plasmonic resonances. Laser & Photonics Reviews, page 1700113.

N'diaye, M. (2017). On the study and development of high-order time integration schemes for ODEs applied to acoustic and electromagnetic wave propagation problems. PhD thesis, Université de Pau et des Pays de l'Adour.

P. Jantsch, C.G. Webster, G. Z. (2016). On the Lebesgue constant of weighted Leja points for Lagrange interpolation on unbounded domains. arXiv:1606.07093.

Sehmi, H. S., Langbein, W., and Muljarov, E. A. (2017). Optimizing the Drude-Lorentz model for material permittivity: Method, program, and examples for gold, silver, and copper. Phys. Rev. B, 95:115444.

Vial, B., Zolla, F., Nicolet, A., and Commandré, M. (2014). Quasimodal expansion of electromagnetic fields in open two-dimensional structures. Phys. Rev. A, 89:023829.

Yan, W., Faggiani, R., and Lalanne, P. (2018). Rigorous modal analysis of plasmonic nanoresonators. Phys. Rev. B, 97:205422.

Zimmerling, J., Wei, L., Urbach, P., and Remis, R. (2016). A Lanczos model-order reduction technique to efficiently simulate electromagnetic wave propagation in dispersive media. J. Comput. Phys., 315:348–362.

Zschiedrich, L., Binkowski, F., Nikolay, N., Benson, O., Kewes, G., and Burger, S. (2018). Riesz-projection-based theory of light-matter interaction in dispersive nanoresonators. Phys. Rev. A, 98:043806.

A Efficiency of interpolation on other cases

In this section, we show the efficiency of the interpolation procedure to reconstruct the field for cases that have been presented in the section 3. The interpolation procedure is described in section 5. Non-dispersive PMLs are used with polynomial eigenvalue solver (PEP) proposed in Slepc. This choice is the most efficient as described in section 4.

A.1 2-D cobra cavity

We consider the cobra cavity introduced in the paragraph 3.1.1 with $r_0 = 250$nm. Nodal finite elements of tenth-order are used for the discretization with 11 111 degrees of freedom for the unknown $\mathbf{E}$. In figure 28, we have displayed the modulus of the electric field on a point of the right section of the cobra for wavelengthes between 500nm and 800 nm. Because of the large

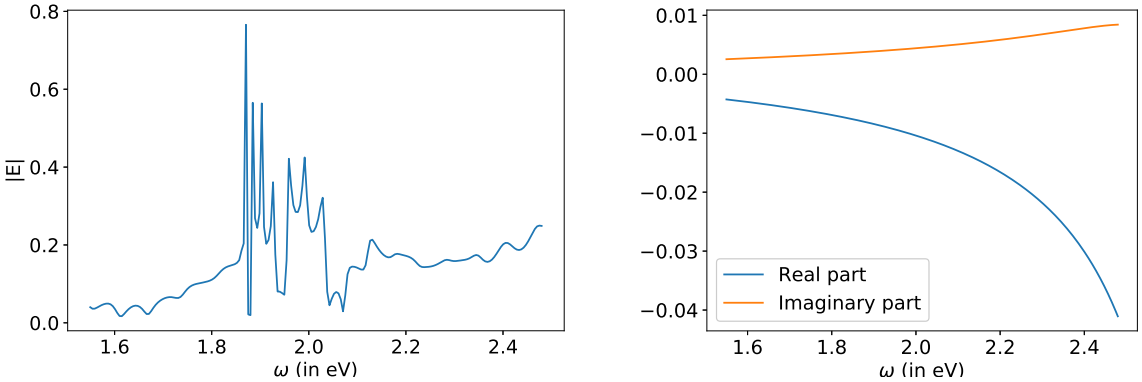

Figure 28: On the left, modulus of electric field at point (5.732 μm, 1.932μm) of the 2-D cobra cavity versus the pulsation ω. On the right, difference between the finite element solution and the modal solution.

number of eigenpulsations close to the real axis (see figure 2), this modulus is highly oscillatory. When we plot the difference $\mathbf{E}^{\text{fem}} - \mathbf{E}^{\text{modal}}$, by computing only 80 modes (located between 0.627eV and 2.725eV), we see that it is slowly varying (right graph of figure 28). As a result, the

Number of points	1	3	5	7	9	13
Error	$9.08 \cdot 10^{-2}$	$1.87 \cdot 10^{-2}$	$1.62 \cdot 10^{-3}$	$4.56 \cdot 10^{-4}$	$2.53 \cdot 10^{-5}$	$6.36 \cdot 10^{-7}$

Table 15: Relative error between the interpolated solution and the finite element solution versus the number of interpolation points. Case of the 2-D cobra cavity with $N = 80$ modes and Leja points.

interpolation procedure works nicely for this case (see table 15). With only five interpolation points, the obtained accuracy is very good. Only 80 modes have been needed to obtain this result whereas the modal solution (without interpolation) requires more than a thousand modes to achieve a similar accuracy (see table 1). Regarding the computation time, the computation of the field for 201 angular frequencies with the interpolation procedure and five interpolation points is completed in 6.72s. A direct computation of the finite element solution (by factorizing

and solving 201 linear systems) requires 69.1s. The simulations have been launched on a single core.

A.2 3-D cobra cavity

We consider the 3-D cobra cavity introduced in the paragraph 3.1.1 with $r_0 = 250$nm. Edge elements of seventh-order are used for the discretization with 467 509 degrees of freedom for the unknown $\mathbf{E}$. In figure 29, we have displayed the modulus of the electric field on a point of the right section of the cobra cavity for wavelengthes between 500nm and 800 nm. Because of the large

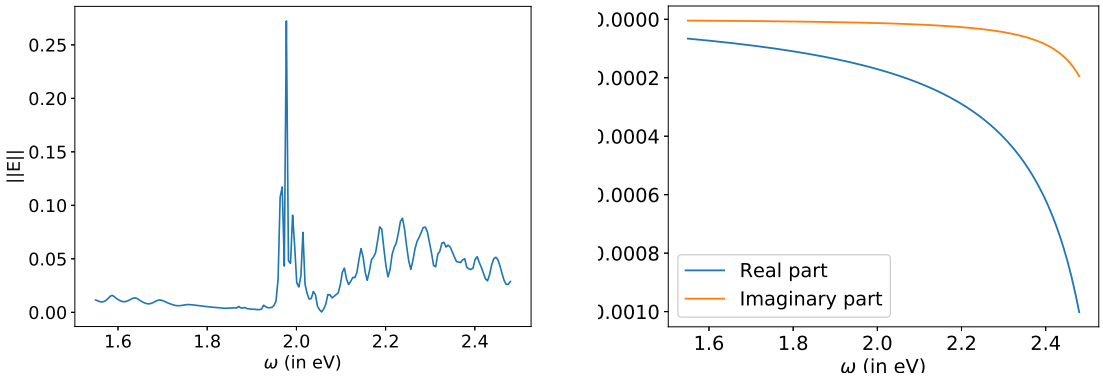

Figure 29: On the left, modulus of electric field at point (5.732 μm, 0.51 μm, 1.932μm) of the 3-D cobra cavity versus the pulsation ω. On the right, difference between the finite element solution and the modal solution (x-component).

number of eigenpulsations close to the real axis (see figure 4), this modulus is highly oscillatory. When we plot the difference $\mathbf{E}^{\text{fem}} - \mathbf{E}^{\text{modal}}$, by computing only 446 modes (located between 0.627eV and 2.597eV), we see that it is slowly varying (right graph of figure 29). Similarly to the

Number of points	1	3	5	7	9	13
Error	$1.79 \cdot 10^{-1}$	$4.82 \cdot 10^{-2}$	$7.62 \cdot 10^{-3}$	$4.06 \cdot 10^{-3}$	$4.28 \cdot 10^{-4}$	$2.57 \cdot 10^{-5}$

Table 16: Relative error between the interpolated solution and the finite element solution versus the number of interpolation points. Case of the 3-D cobra cavity with $N = 446$ modes and Leja points.

2-D case, the interpolation procedure works correctly for this case. The number of modes needed is larger, since the 3-D cobra cavity has a larger number of modes. The interpolation procedure is computationally efficient since it computes the solution for 201 angular frequencies in 742s while a direct computation needs 4880s to be completed. The simulations have been launched on 16 cores.

A.3 Silica square

We consider the dielectric square of paragraph 3.1.2 with an incident plane wave. Nodal finite elements of tenth order are used with 19 881 degrees of freedom for the unknown $\mathbf{E}$. In figure

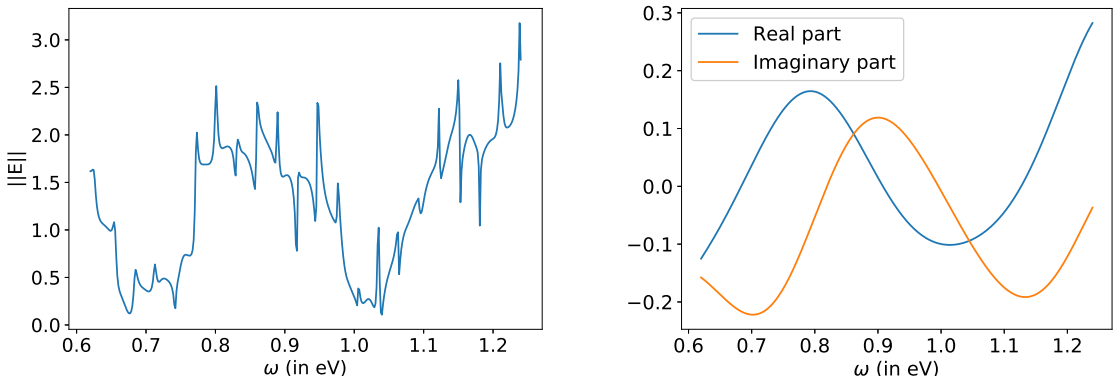

Figure 30: On the left, modulus of electric field at point (2.4 μm, 3.6 μm) of the dielectric square $[-5\mu m, 5\mu m]^2$ versus the pulsation ω. On the right, difference between the finite element solution and the modal solution.

30, the modulus of the electric field is represented. Because of the large number of quasi-normal modes (cf. figure 9) in the considered range of frequencies (401 wavelengthes between 1μm and 2μm), this modulus exhibits numerous peaks. However, the difference between the modal solution with $N = 836$ modes and the finite element solution is smooth (right graph of figure 30). Compared to the cobra cavity, the frequency range is larger, that's why the difference presents

Number of points	1	3	5	7	9	11
Error	$2.88 \cdot 10^{-1}$	$2.92 \cdot 10^{-1}$	$2.82 \cdot 10^{-1}$	$2.92 \cdot 10^{-1}$	$5.73 \cdot 10^{-2}$	$1.48 \cdot 10^{-2}$

Number of points	13	15	17	19	21
Error	$1.77 \cdot 10^{-3}$	$1.32 \cdot 10^{-4}$	$4.23 \cdot 10^{-5}$	$1.44 \cdot 10^{-5}$	$5.74 \cdot 10^{-6}$

Table 17: Relative error between the interpolated solution and the finite element solution versus the number of interpolation points. Case of the 2-D dielectric square with $N = 836$ modes and Leja points.

more oscillations. As a result, the interpolation procedure provides an error that stagnates for a small number of interpolation points (cf. table 17). From seven interpolation points, we recover the exponential convergence as expected. The interpolation procedure is computationally efficient since it computes the solution for 401 angular frequencies in 47s (with 13 interpolation points) while a direct computation needs 67s to be completed. The simulations have been launched on 8 cores.

A.4 Germanium disk

We consider the germanium disc introduced in the paragraph 3.2.1 with an incident plane wave. Nodal finite elements of tenth-order are used for the discretization with 5 131 degrees of freedom for the unknown **E**. In section 3.2.1, sixth-order finite elements were used with the same mesh. We have chosen to increase the order of approximation in order to obtain a solution more accurate, the numerical error is around 10^{-4}. In figure 31, we have displayed the modulus of the electric field on a point of the computational domain for wavelengthes between 500nm and 1.3 μm. The

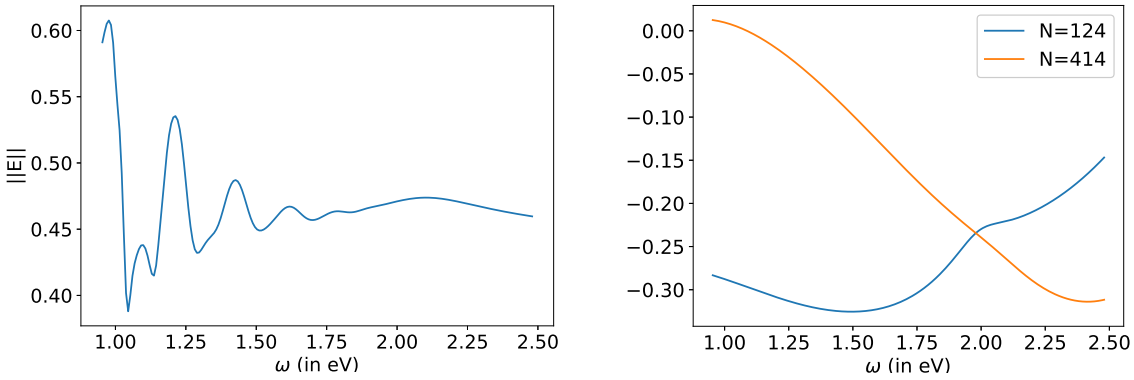

Figure 31: On the left, modulus of electric field at point (-200 nm, 800 nm) of the germanium disc versus the pulsation ω. On the right, difference between the real part of the finite element solution and the modal solution (for 124 or 414 modes).

modal solution is computed either with 124 modes or 414 modes, the selected eigenpulsations are given in figure 32. When we plot the difference $\mathbf{E}^{\text{fem}} - \mathbf{E}^{\text{modal}}$, by computing only 124 modes,

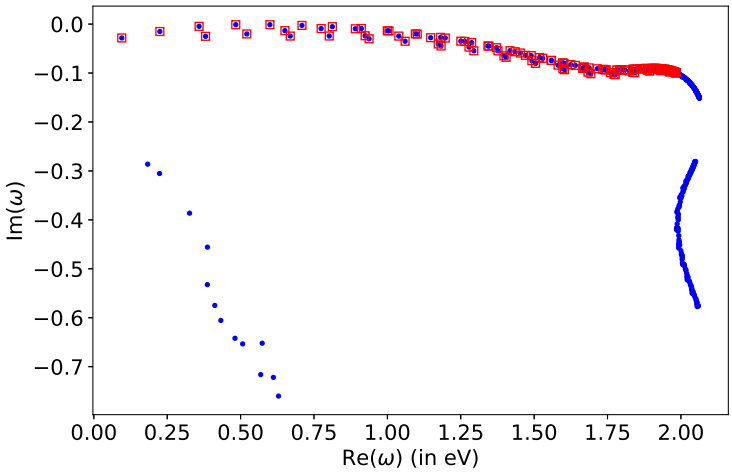

Figure 32: Eigenpulsations for the germanium disc (124 modes as red squares, 414 modes as blue points).

we see that it is slowly varying (right graph of figure 31) except around 2eV which coincides with a pole and zero of the permittivity. Indeed the permittivity chosen (see table 4) admits a pole at $\omega = 2.07938 - 0.19684i(eV)$ and a zero at $\omega = 2.05074 - 0.28031i(eV)$. By taking much more eigenpulsations close to these two points, we see that we can get rid of this strong variation for $\omega \approx 2eV$. As a result, the interpolation procedure works better when 414 modes are selected (see table 18). With only five interpolation points, the obtained accuracy is good. By selecting 124 modes, more interpolations points are needed. Regarding the computation time,

Number of points	1	3	5	7	9	13
Error ($N = 124$)	$4.12 \cdot 10^{-1}$	$5.73 \cdot 10^{-2}$	$1.66 \cdot 10^{-2}$	$1.56 \cdot 10^{-2}$	$1.03 \cdot 10^{-2}$	$6.38 \cdot 10^{-3}$
Error ($N = 414$)	$3.92 \cdot 10^{-1}$	$5.06 \cdot 10^{-2}$	$3.59 \cdot 10^{-3}$	$2.34 \cdot 10^{-3}$	$8.34 \cdot 10^{-4}$	$2.98 \cdot 10^{-4}$

Table 18: Relative error between the interpolated solution and the finite element solution versus the number of interpolation points. Case of the germanium disc with $N = 124$ modes or $N = 414$ modes and Leja points.

the computation of the field for 201 angular frequencies with the interpolation procedure and five interpolation points and $N = 414$ modes is completed in 130s. If we select 13 interpolation points and $N = 124$ modes, the computation is completed in 32s. A direct computation of the finite element solution (by factorizing and solving 201 linear systems) requires 37.5s. For this case, it is more efficient to select a limited number of modes. The simulations have been launched on a single core.

A.5 Germanium sphere

We consider the germanium sphere introduced in the paragraph 3.2.2 with an incident plane wave. Edge elements of fourth-order are used for the discretization with 46 672 degrees of freedom for the unknown $\mathbf{E}$. Compared to the section 3.2.2, the mesh is two times finer (each hexahedron is split into eight small hexahedra). We have chosen to refine the mesh in order to obtain a solution more accurate, the numerical error is around $5 \cdot 10^{-4}$. In figure 33, we have displayed the modulus of the electric field on a point of the computational domain for wavelengthes between 600nm and 1.2 μm. The modal solution is computed with only 20 modes.

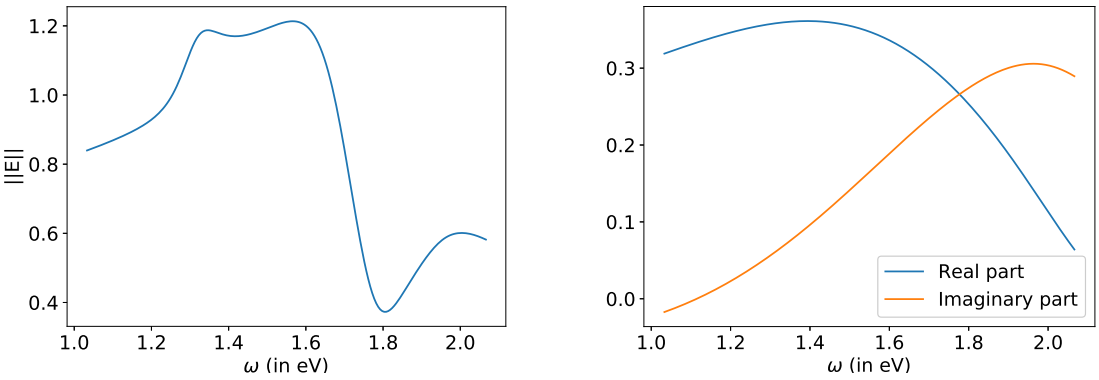

Figure 33: On the left, modulus of electric field at point (90 nm, 0, 90 nm) of the germanium sphere versus the pulsation ω. On the right, difference between the real part of the finite element solution and the modal solution with N=20 modes.

Compared to the germanium disk, the sphere is here much smaller, that's why there are less modes close to the real axis. When we plot the difference $\mathbf{E}^{\text{fem}} - \mathbf{E}^{\text{modal}}$, by computing only 20 modes, we see that it is slowly varying (right graph of figure 33) except around 2eV which coincides with a pole and zero of the permittivity. The interpolation procedure works fine (see table 19). With only seven interpolation points, the obtained accuracy is good. Regarding the computation time, the computation of the field for 201 angular frequencies with the interpolation

Number of points	1	3	5	7	9	13
Error	$7.81 \cdot 10^{-1}$	$5.70 \cdot 10^{-2}$	$8.32 \cdot 10^{-3}$	$3.18 \cdot 10^{-3}$	$8.34 \cdot 10^{-4}$	$9.94 \cdot 10^{-5}$

Table 19: Relative error between the interpolated solution and the finite element solution versus the number of interpolation points. Case of the germanium sphere with $N = 20$ modes and Leja points.

procedure and seven interpolation points is completed in 27s. A direct computation of the finite element solution (by factorizing and solving 201 linear systems) requires 218s. The simulations have been launched on 8 cores.

B Displacement of roots and poles of the permittivity function

In this section, we propose a strategy in order to avoid the proximity of poles or zeros of $\varepsilon(\omega)$ to the real axis. Indeed, if the poles or roots of $\varepsilon(\omega)$ are close to the real axis, we have seen in section 3 that it will increase the number of modes required to obtain an accurate modal solution. It is an also an issue if the interpolation procedure described in 5 is used because the eigensolver may fail to compute the eigenpulsations close to the interval $[\omega_1, \omega_2]$ on the real axis because of accumulation of eigenpulsations on roots or poles of $\varepsilon(\omega)$. The number of modes close to the interval $[\omega_1, \omega_2]$ can also be very large. In order to control the position of the poles or roots, we search ε with the following expression

$$\varepsilon(\omega) = \varepsilon_\infty \frac{(\omega - R_1)(\omega + \bar{R}_1) \cdots (\omega - R_n)(\omega + \bar{R}_n)}{(\omega - \Omega_1)(\omega + \bar{\Omega}_1) \cdots (\omega - \Omega_n)(\omega + \bar{\Omega}_n)} \tag{15}$$

where R_i are roots of $\varepsilon(\omega)$ and Ω_i poles of ε. If Ω_i is a pole, we impose that $-\bar{\Omega}_i$ is also a pole and similarly for roots. With this approach, the permittivity given by equation (15) is causal. The parameters $\varepsilon_\infty, R_1, R_2, \cdots, R_n, \Omega_1, \Omega_2, \cdots, \Omega_n$ are searched such that the quantity $\varepsilon(\omega) - \varepsilon_{\text{mes}}(\omega)$ is minimized where ε_{mes} is the measured permittivity. We can minimize this quantity under constraints such that

$$\text{Im}(R_i) \leq -0.5, \quad \text{Im}(\Omega_i) \leq -0.5 \tag{16}$$

in order to keep poles and root far enough from the real axis. The minimization under constraints is performed with least_squares function of python.scipy. The minimization is launched with random initial guesses, we select the optimal parameters among a thousand runs. In figure 34, we represented the measured permittivity for the germanium and different approximations :

- No bounds : there are no constraints on parameters, we choose $n = 2$.
- n poles : the minimization is performed with n poles (and their conjugates) with the constraints (16)

We can see that sharp variations of ε are more difficult to approximate accurately if constraints are imposed. When no constraints are set, we obtain a relative L^2 error (in the interval [0.3eV, 2.5eV]) of 1.92 % with n=2. With the constraints (16), the L^2 error is equal to 4.63 %, 3.43 %, 2.71 % and 2.33 % for n=2, 3, 4 and 5 respectively. In tables 20 and 21, we provide the parameters ε_∞, R_i, Ω_i for n=2 and n=5. We can observe that numerous parameters Ω_i or R_i have an imaginary part equal to -0.5 which corresponts to the upper bound of constraint (16).

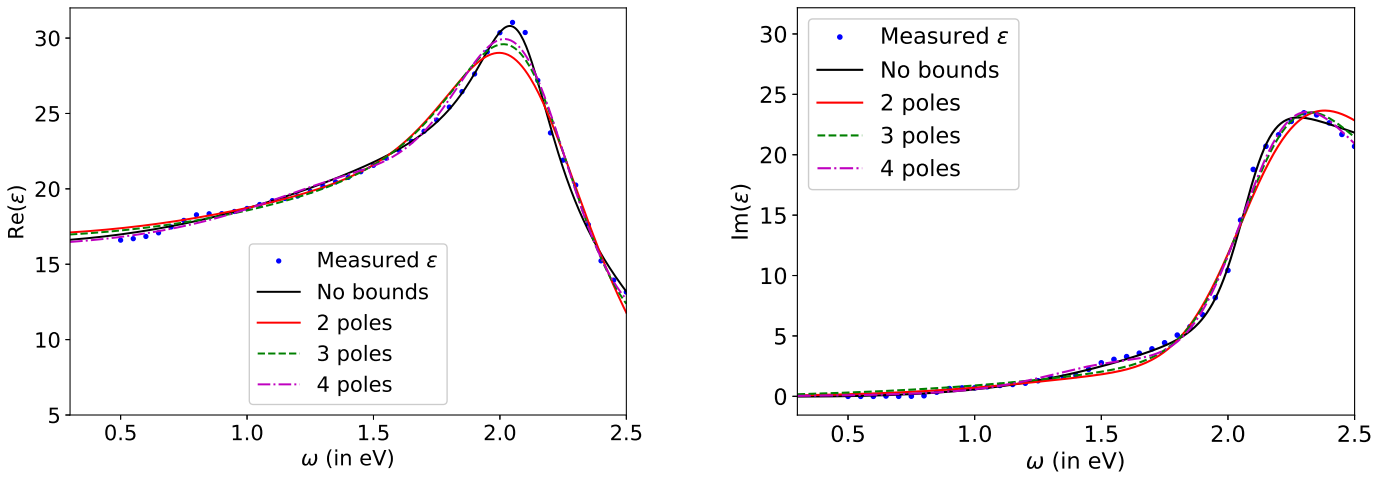

Figure 34: On the left real part of $\varepsilon(\omega)$, on the right imaginary part (germanium). We show the measured permittivity, the obtained permittivity when no bounds are prescribed for the parameters (i.e. no constraints), and the permittivity obtained by constraining the parameters with n=2, 3, 4.

ε_∞	$\mathrm{Re}(R_1)$	$\mathrm{Im}(R_1)$	$\mathrm{Re}(\Omega_1)$	$\mathrm{Im}(\Omega_1)$
5.50488573	3.52354416	-2.12375772	2.07954764	-0.5

$\mathrm{Re}(R_2)$	$\mathrm{Im}(R_2)$	$\mathrm{Re}(\Omega_2)$	$\mathrm{Im}(\Omega_2)$
1.74885098	-0.5	1.87010153	-0.69106174

Table 20: Parameters for the germanium with $\mathrm{Im}(R_i) \leq -0.5$, $\mathrm{Im}(\Omega_i) \leq -0.5$ and n=2.

ε_∞	$\mathrm{Re}(R_1)$	$\mathrm{Im}(R_1)$	$\mathrm{Re}(\Omega_1)$	$\mathrm{Im}(\Omega_1)$	$\mathrm{Re}(R_2)$	$\mathrm{Im}(R_2)$
2.45352827	2.48266876	-0.55333114	1.6010841	-0.50349749	5.88696178	-3.59561585

$\mathrm{Re}(\Omega_2)$	$\mathrm{Im}(\Omega_2)$	$\mathrm{Re}(R_3)$	$\mathrm{Im}(R_3)$	$\mathrm{Re}(\Omega_3)$	$\mathrm{Im}(\Omega_3)$	$\mathrm{Re}(R_4)$
2.15350011	-0.5	2.46992867	-0.50000008	2.15262651	-0.50000002	1.76296625

$\mathrm{Im}(R_4)$	$\mathrm{Re}(\Omega_4)$	$\mathrm{Im}(\Omega_4)$	$\mathrm{Re}(R_5)$	$\mathrm{Im}(R_5)$	$\mathrm{Re}(\Omega_5)$	$\mathrm{Im}(\Omega_4)$
-0.5	3.14808755	-0.50115937	1.76296605	-0.50000005	2.15152138	-0.5

Table 21: Parameters for the germanium with $\mathrm{Im}(R_i) \leq -0.5$, $\mathrm{Im}(\Omega_i) \leq -0.5$ and n=5.

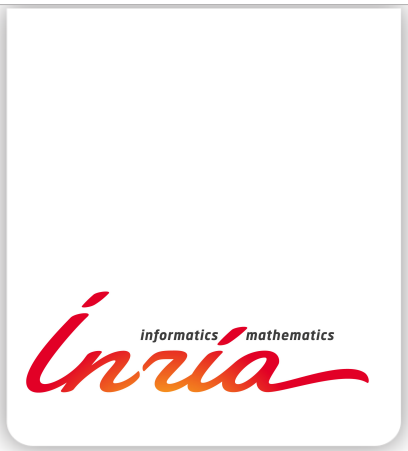

RESEARCH CENTRE
BORDEAUX – SUD-OUEST

200 avenue de la Vieille Tour
33405 Talence Cedex

Publisher
Inria
Domaine de Voluceau - Rocquencourt
BP 105 - 78153 Le Chesnay Cedex
inria.fr

ISSN 0249-6399